Mouse Skeletal Muscle Decrease in the MICOS Complex and Altered Mitochondrial Networks with age

Zer Vue*, Edgar Garza-Lopez*, Kit Neikirk*, Larry Vang, Heather Beasley, Jianqiang Shao, Andrea G. Marshall, Amber Crabtree, Chantell Evans, Brittany Taylor, Trace A. Christensen, Jacob Lam, Benjamin Rodriguez, Mark A. Phillips, Jamaine Davis, Anilkumar K. Reddy, Anita M. Quintana, Sandra A. Murray, Vernat Exil, Bret C. Mobley, Jose A. Gomez#, Dao-Fu Dai#, Antentor Hinton, Jr#

Affiliations:
Z.V., K.N., L.V., H.B., A.G.M., J.A.G., A.H.J.: Department of Molecular Physiology and Biophysics, Vanderbilt University, Nashville, TN, 37232, USA.
E.G., J.L., B.R.: Department of Internal Medicine, University of Iowa, Iowa City, IA, 52242, USA.
J.S.; Central Microscopy Research Facility, University of Iowa, Iowa City, IA, 52242, USA.
C.E.: Department of Cell Biology, Duke University School of Medicine, Durham, NC, 27708, USA.
B.T.; J. Crayton Pruitt Family Department of Biomedical Engineering, University of Florida, Gainesville, FL, 32611, USA
T.A.C.:Microscopy and Cell Analysis Core Facility, Mayo Clinic, Rochester, MN, 55905, USA.
M.A.P.: Department of Integrative Biology, Oregon State University, Corvallis, OR, 97331, USA.
J.D.: Department of Biochemistry, Cancer Biology, Neuroscience, and Pharmacology, Meharry Medical College, Nashville, TN 37208, USA.
A.M.Q.: Department of Biological Sciences, University of Texas at El Paso, El Paso, TX, 79968, USA.
V.G.: Department of Cell and Developmental Biology, Vanderbilt University, Nashville, TN, 37232, USA.
S.A.M: Department of Cell Biology, School of Medicine, University of Pittsburgh, Pittsburgh, PA, 15260, USA.
V.E.: Department of Pediatrics, Carver College of Medicine, University of Iowa, Iowa City, IA. 52242, USA.
A.K.R.: Department of Medicine, Baylor College of Medicine, Houston, TX, 77001.
V.E.: Department of Pediatrics, Div. of Cardiology, St. Louis University School of Medicine, St. Louis, MO, 63104, USA.
B.M.: Department of Pathology, Vanderbilt University Medical Center, Nashville, TN, 37232 USA.
J.A.G.: Department of Medicine, Vanderbilt University Medical Center, Nashville, TN, 37232, USA
D.D.: Department of Pathology, Carver College of Medicine, University of Iowa, Iowa City, IA, 52242, USA.

*These authors share co-first authorship.
#These authors share senior authorship.

Corresponding Author:
Antentor Hinton
Department of Molecular Physiology and Biophysics
Vanderbilt University
antentor.o.hinton.jr@Vanderbilt.Edu 319-383-3095

Graphical Abstract:

ABSTRACT

Skeletal muscle gradually loses mass, strength, endurance, and oxidative capacity during aging. While mitochondrial aging is associated with endoplasmic reticulum stress, fragmented mitochondria, and decreased mitochondrial capacity, the genes associated with morphological changes in mitochondria during aging still requires further elucidation. Further, it is not completely understood how 3D mitochondrial networks and the specialization of mitochondria are altered during aging. We measured changes in mitochondrial morphology and mitochondrial connectivity during the aging of the mouse gastrocnemius muscle through serial block facing-scanning electron microscopy and 3D reconstruction. We found changes in mitochondrial network configuration, nanotunneling, size, shape, number, contact sites, cristae organizing system (MICOS) dynamics and gene expression in skeletal muscle during aging. We also found an association of OPA-1 and the MICOS complex in the gastrocnemius with mitochondrial aging. Further, the loss of the MICOS complex was linked with decreased oxidative capacity and altered mitochondrial metabolism. MICOS proteins decreased with age and mitochondrial morphology was similar between aged skeletal muscle and that of young mice with MICOS protein loss. In tandem, our data suggest a relationship between the MICOS complex and aging, which could be potentially linked to disease states with additional 3D reconstruction.

Keywords: MICOS, aging, mitochondria, 3D morphometry; mitochondrial disease; mitochondrion; nanotunnel; reconstruction; reticulum; serial block-face SEM; skeletal muscle.

INTRODUCTION

The loss of muscle mass associated with aging, known as sarcopenia, impacts the quality of life affecting both type I and type II fibers, but more so for type II fibers. The mitochondrial free radical theory of aging (MRFTA) which proposes that the accumulation of reactive oxygen species (ROS) byproducts causes damage that leads to aging [1–3]. The critical role of mitochondrial oxidative stress in aging has been shown using mitochondrial-targeted antioxidants, such as catalase targeted to mitochondria, in cardiac aging [4] and sarcopenia [5]. In addition to the main function of generating cellular ATP by oxidative phosphorylation [6], the mitochondria play critical role in ROS signaling, calcium homeostasis, programmed cell death, and regulation of innate immunity and stem cells. To carry out the tremendous variety of tasks, mitochondria maintain finely regulated ultrastructures, through various mechanisms, one of which is mitochondrial dynamic machinery through fission and fusion. Since their structure changes dynamically as mitochondria shift from fission to fusion, many important mitochondrial functions depend on their ultrastructure[7–9], therefore, it is important to understand mitochondrial structural changes over time. Essential mitochondrial functions are associated with the mitochondrial inner membrane folds known as cristae, which house the oxidative phosphorylation machinery[8] and various transporters. Our objective was to determine how mitochondrial networks and individual mitochondrial structures change during aging. We hypothesized that age-related oxidative stress causes increased mitochondrial mitophagy and fragmentation over time with concomitant losses in mitochondrial cristae integrity.

Disruption of optic atrophy 1 (OPA-1), an inner membrane protein that regulates mitochondrial fusion, causes mitochondrial fragmentation and affects the dimensions, shapes, and sizes of the cristae [8]. Disruption of Drp1, a protein associated with mitochondrial fission, causes elongated mitochondria and resistance to remodeling of the cristae [10,11]. Nanotunnels or "mitochondria-on-a-string" are thin, double-membrane protrusions lacking cristae that allow mitochondria to communicate across distances. Nanotunnels may increase in mitochondrial disease [12,13] and may be associated with mitochondrial dysfunction during aging. Mutations in genes that regulate the morphology of cristae have been associated with aging cardiomyocytes [14]. These gene products are located at the crista junctions in the inner membrane and are a part of the mitochondrial contact site and cristae organizing system (MICOS), which are important for maintaining mitochondrial shape and size [15]. DRP1 or OPA-1 loss can similarly affect mitochondria morphology [16,17]. Cristae membranes contain the electron transport chain complexes and ATP synthase for ATP synthesis via oxidative phosphorylation [18–20]. Since mitochondrial morphology affects function, altering the structure by knocking out MICOS-associated genes or the GTPase of OPA-1 could alter the metabolism and function of mitochondria during aging [18–20]. Critically, we predicted that MICOS-associated genes were lost over age, therefore, loss of MICOS-associated genes would mimic loss in mitochondria morphology observed across age.

To better understand the alterations of mitochondrial specialization ultrastructure in aging, we compared size, shape, quantity, complexity, and branching of mitochondria using 3D reconstructions of aged gastrocnemius, and we measured nano tunneling in mouse muscles at these three ages. Multivariate analysis was used to identify changes in metabolites, the MICOS complex, OPA-1, nano tunneling, mitochondrial complexity, and morphological changes to better understand how mitochondrial specialization and structure change during aging.

RESULTS

Aging Results in Smaller, Shorter, Poorly Connected Mitochondria with Decreased Branching in Mouse Skeletal Muscle

The gastrocnemius is a mixed muscle with both oxidative fibers containing many mitochondria and glycolytic fibers with few mitochondria. This heterogeneity makes the gastrocnemius ideal to study changes in mitochondrial dynamics. Since many mitochondrial functions depend on structure [7–9], it is important to examine mitochondrial structural changes over time. We hypothesized that increasing mitochondrial mitophagy and fragmentation over time is concomitant with losses in mitochondrial crista integrity.

Our objective was to determine how aging alters mitochondrial networks and individual mitochondrial structure. We imaged gastrocnemius biopsies from young (3-month-old), mature (1-year-old) and aged (2-year-old) mice by serial block-face scanning electron microscopy (SBF-SEM) with resolutions of 10 µm for the x- and y- planes and 50 µm for the z-plane, which allows visualization of the electron connectome. Approximately 50 intermyofibrillar (IMF) mitochondria were segmented from each image stack (Figure 1A-C) and a 3D surface view was generated (Figure 1A''-C''). We analyzed mitochondria sub-network volumes from four ROIs with an average of 175 mitochondria for each mouse (n = 3), for a total of 500 mitochondria. Mitochondrial networks in aged mice showed largely interconnected mitochondria that were not composed of a single reticulum (Figures 1A'''–C'''). We found that mitochondrial volume decreased with age (Figures 1 A'''–C'') as did mitochondrial network volumes (Figure 1D). The area and perimeter of mitochondria of samples from 2-year-old mice were significantly lower than those from 3-month-old mice; however, there was no significant change for 1-year-old mice compared to 3-month-old mice (Figures 1E-F). While there was some variability across the three mice for each age cohort (SFigure 1), in general the trend showed a downwards trajectory emblematic of increased fragmentation and smaller mitochondria. This showed that the size and length of mitochondria change with age, but the specific complexity of mitochondria, which is implicated with mitochondria communication, needed to be further elucidated.

We next measured mitochondrial complexity to better understand changes in mitochondrial shape during aged mitochondrial complexity, quantification of the 2D form factor as a 3D shape, as above. We hypothesize that less networks and simpler shape would occur as aging and dysfunction continued. Previously established methods [21,22] were used to determine three dimensional mitochondrial complexity from two dimensional form factor measurements [21,22]. First, we first examined transverse (Figure 2A-C) and longitudinal (Figure 2A'-C') mitochondrial dimensions across ages in skeletal muscle. These measures showed networking and broad mitochondria. Mitochondrial branching index (MBI) is the ratio of transverse (Figures 2A–C) to longitudinal (Figures 2A'-C') branching, which better quantifies the orientation of the branching, and MCI and MBI together measure mitochondria morphology [21]. We found that MBI decreased across the age cohorts (Figure 2D). Since we observed in 3D reconstructions that mitochondrial populations are heterogeneous and diverse, we utilized mito-typing, which is the karyotyping-like method for arranging mitochondria [21], to capture the diversity of IMF mitochondria (Figure 2E). This analysis suggested at every volumetric measurement, mitochondria were smaller and less complex with age. We also measured sphericity to further understand changes in complexity. There was a progressive increase in sphericity with aging (Figure 2F). When examining the specific three male mice sampled for each age cohort, some variation exists for both metrics; however, the trends again clearly show sphericity stays consistent while MBI decreases across age (SFigure 2). Together, these data suggest that complexity decreases across all mitotypes with age.

Mitochondrial Nanotunnels Change in Size and Amount with Aging in Skeletal Muscle

To quantify nanotunnels in skeletal muscle, we performed 3D reconstruction in mice at three ages, measuring 550 mitochondria per mouse (n=3) using four different regions of interests (ROIs). Although nanotunnels are reported to exist primarily in mitochondrial disease states [12], we found them in all three ages of mice (Figures 3A–C). The diversity and heterogeneity in the organization, sizing, and branching of nanotunnels necessitated mito-otyping (Figure 3D). We found nanotunnels in a greater proportion of mitochondria in 1-year-old mice than in 2-year-old mice (Figure 3E). However, the number of nanotunnels in each mitochondrion was significantly less in the 2-year-old mice than the 3-month-old and 1-year-old mice (Figure 3F). The length and diameter of nanotunnels increased in the older mice compared to the 3-month-old mice (Figures 3G–H), but the increase was significantly greater in the 1-year-old mice than the 2-year-old mice (Figures 3G–J). These data show that nanotunnel structure, frequency, and length change during aging.

Since we observed mitochondrial dynamics and cristae change with aging , we measured transcripts for *Opa-1*, the gene associated with mitochondrial fusion, and *CHCHD3* (*Mic19*), *CHCHD6* (*Mic25*), and *Mitofilin* (*Mic60*), the genes for the principal MICOS complex subunits. We used reverse-transcriptase qPCR (RT-qPCR) to determine the effect of aging on transcription. Since aging causes fragmentation of mitochondria, a hallmark for this process is loss of *Opa-1* and MICOS complex proteins. We hypothesized that aging would also lead to decreases in the associated MICOS complex proteins, confirming prior studies which have found Opa-1 loss across aging [19,23–25]. We found progressive loss of both *Opa-1* and MICOS complex subunits, as measured by loss of transcripts for the proteins (SFigure 3A–D). In 1- and 2-year-old mice, the amount of mRNA made for the MICOS complex subunit genes or the *Opa-1* gene was less than half of that made in 3-month-old mice (SFigure 3A–C). Furthermore, for all MICOS genes, there was a statistically significant decrease in the amount of mRNA over time with a higher level of significance in 2-year-old mice. These data suggest a correlation between mitochondrial morphologic changes and decreases in expression of genes for *Opa-1* and MICOS subunits *CHCHD3*, *CHCHD6*, and *Mitofilin* during aging; however, they are not sufficient to demonstrate causation, therefore we did additional measurements to show that reduced protein expression levels may be responsible for the morphologic changes.

Changes in Cristae and Mitochondria in Myotubes and Oxygen Respiration Rate Upon Knockout of MICOS complex and *Opa-1*

The MICOS complex and OPA-1 are key players in mitochondrial biogenesis [15,19,26], but how their interactions regulate aging and mitochondrial ultrastructures is poorly understood. To determine the role of OPA-1 and the MICOS complex in mitochondrial structure and networking, we ablated the genes for *Opa-1* and the MICOS complex in isolated primary skeletal muscle cells from 3-month-old mice. We isolated primary satellite cells, then differentiated myoblasts to myotubes. Using CRISPR/Cas9 method (Table 2), and a control plasmid, we knocked out the genes for MICOS complex components and *Opa-1* from skeletal muscle cells. As observed previously, in vitro deletion of OPA-1 altered mitochondrial morphology [16,27,28]. We measured 1250 mitochondria across 10 cells, with loss of *Opa-1* as a positive control for mitochondrial morphological changes. Although *Opa-1* expression decreases with age [29], the effect of the MICOS complex being lost in mitochondria morphology is unknown. Using transmission electron microscopy (TEM) images, we compared mitochondria and cristae in

myotubes from wild type (WT) and knockouts of *Opa-1* and *Mitofilin* genes, which are essential for the organization of mitochondrial cristae [30,31] (Figures 4A–C). Mitochondrial average area decreased for both *Opa-1* and *Mitofilin* knockout myotubes (Figure 4D), while mitochondrial circularity (the roundness and symmetry of mitochondria) and number increased for both *Opa-1* and *Mitofilin* knockout myotubes (Figures 4E–F). For both *Opa-1* and *Mitofilin* knockouts, the number of cristae per mitochondrion decreased, as did the cristae score and cristae surface areas compared to the WT (Figures 4G–I). Cristae score measures the uniformity and regularity of cristae compared to typical cristae, with a lower number representing abnormality and dysfunction.

To further elucidate these changes in event of loss of other MICOS proteins, we also compared WT with *Opa-1*, *CHCHD3*, and *CHCHD6* knockout myotubes (Figures 5A–D). Knockout of MICOS subunit *CHCHD3* results in fragmented mitochondria with less *Opa-1* as the cristae lose their normal structure [32]. Similarly, *CHCHD6* is important in maintaining crista structure and its downregulation results in hollow cristae lacking an electron-dense matrix, thereby inhibiting ATP production and cell growth [31,33,34]. Mitochondrial average area decreased for *Opa-1*, *CHCHD3*, and *CHCHD6* knockout myotubes (Figure 5E), while the circularity index and the number of mitochondria, once normalized, increased (Figures 5F–G). For *Opa-1*, *CHCHD3*, and *CHCHD6* knockouts, the number of cristae per mitochondrion decreased, as did the cristae score and cristae surface area compared to the WT (Figures 5H–J). The least significant change was seen in the *CHCHD3* knockout. Together, these data show quantitative and structural changes in both mitochondria and cristae upon loss of MICOS proteins.

Loss of OPA-1 induces bioenergetic stress and decreased electron transport chain function [28] and ablation of the MICOS complex alters mitochondrial capacity [35,36]. We found that loss of OPA-1 or *Mitofilin* in myotubes decreased basal oxygen consumption rate (OCR) (Figures 4J–K) and decreased ATP-linked, maximum, and reserve capacity OCR (Figures 4L–N). Although OPA-1 knockout myotubes exhibited a decrease in proton leak, which represents protons that go from the mitochondria to matrix without producing ATP, *Mitofilin* knockouts showed no significant difference (Figure 4O). In *Opa-1*, *CHCHD3*, and *CHCHD6* knockouts, there was a decrease in basal, ATP-linked, maximum, and reserve capacity OCR compared to the control (Figures 5K-O). Although proton leak OCR decreased in *Opa-1* and *CHCHD3* knockout myotubes (Figure 5P), there was no significant difference between the control and *CHCHD6*. The decrease in OCR may be attributed to smaller and fragmented mitochondria; mitochondrial density decreases as fragmentation targets them for autophagy [29,37]. Together, these results show that MICOS and *Opa-1* are essential for normal respiration of muscle tissue.

TEM provides mitochondrial detail, but not 3D morphology; therefore, we used SBF-SEM to look at the 3D structure of the mitochondria. Using myotubes with ablated genes for *Opa-1* and MICOS complex subunits, as described above, we measured a total of 200 mitochondria across 10 cells. We compared mitochondria in WT, *Opa-1*, *Mitofilin, CHCHD3*, and *CHCHD6* knockout myotubes (Figures 6A-E).

We found that compared to the elongated mitochondria in the WT, the 3D length was much shorter in *Opa-1* and MICOS protein knockouts (Figure 6F). Similarly, the volume of mitochondria was also less in *CHCHD3*, *CHCHD6*, *Mitofilin*, and *Opa-1* knockouts compared to the control (Figure 6G). The 3D reconstruction data, in combination with the prior TEM results, show how mitochondrial dynamics change with the loss of MICOS subunits.

Metabolomics Show Key Metabolite Changes in Knockout of MICOS Complex Proteins and *Opa-1* in Myotubes.

To determine the global effects of loss of *Opa-1* or the MICOS complex in skeletal muscle myotubes, we analyzed the metabolome to identify changes in metabolites that occurred with changes in mitochondria and cristae. Principal component analysis (PCA) revealed distinct populations in the control and the *Mitofilin* knockout strains, which suggested that their genotypes contributed to the clustering (SFigure 4A). To identify metabolites with the most robust ability to discriminate between true positives and false positives, we constructed a model using analysis of variance (ANOVA) to determine several key metabolites that were statistically significant (SFigure 4B). This unique metabolite signature revealed that *Mitofilin* plays a critical role in regulating amino acid metabolism and steroidogenesis (SFigure 4C–D). Upregulation of steroidogenesis pathways may result from the increased fluidity of membranes caused by *Mitofilin* [38,39]. We also measured the effect of ablation of genes for *CHCHD3* and *CHCHD6* in skeletal muscle myotubes on bioenergetic metabolism. PCA revealed distinct populations in the control and the *CHCHD3* and CHCHD6 knockouts, which showed a similar profile (SFigure 5A). We constructed a model using ANOVA to determine which metabolite changes in *CHCHD3* and *CHCHD6* knockouts were statistically significant (SFigure 5B) There was a loss of protein synthesis and changes in carbohydrate metabolism (SFigure 5C–D). Loss of *Opa-1* typically favors fatty acid synthesis, so these results showing increased carbohydrate metabolism differ from previous *Opa-1* knockout responses [40–42]. This atypical response was evident in the increase in lactose and starch synthesis, but there was poor protein turnover, as seen in methionine metabolism (SFigure 5D).

DISCUSSION

We demonstrated that either aging or loss of MICOS proteins in skeletal muscle resulted in suboptimal mitochondria morphology, suggesting a correlation between aging and MICOS protein expression. Previous studies used 3D focused ion beam-scanning electron microscopy (FIB-SEM) to characterize the networking of the mitochondria in human[43] and mouse skeletal muscle[44]. Another report did quantitative 3D reconstructions using SBF-SEM to define the morphological differences in the skeletal muscles of humans versus mice, and they compared patients with primary mitochondrial DNA diseases with healthy controls[21]. To the best of our knowledge, our current study is the first to use 3D reconstruction method as a novel approach to study the connections between mitochondria and to determine how disconnections and reduced mitochondrial communication altered in skeletal muscle aging.

Skeletal muscle highly mitochondrial dependent as well as mitochondria enriched and is highly enriched in , which comprise ~6% of the cell volume and is well known to change with aging[45]. Gastrocnemius muscle has both type I slow-twitch muscle fibers and type II fast-twitch muscle fibers; type I fibers are more effective for endurance, while type II fibers better support short bursts of muscle activity [45–47]. Our 3D morphologic data, however, did not permit discrimination of the two fiber types, although we observed many variable muscle fibers within a sample and between all differently aged cohorts. Futures studies may develop novel methods that are able to distinguish fiber types to determine the changes in mitochondria. Past studies in human skeletal muscle did this by taking two portion of samples and assessing fiber type via SDS-PAGE [48].

Using 3D reconstructions, we found that all parameters of the mitochondria changed during aging including smaller volume, area, and perimeter (Figure 1D-F), and the mitochondria became less interconnected. This increased fragmentation suggests a decreased mitochondrial fusion, in association with age-dependent decreases of OPA-1, which is a regulator of mitochondrial fusion. We also saw a decrease in the MBI during aging, suggesting that mitochondria decrease in networking, but their shape may not radically change as they increase in sphericity as they age (Figure 2).

The change in morphology in aging mitochondria could be explained by the MFRTA, which proposes that ROS alter other functions of mitochondria, including ATP production, as they induce aging [49]. Since oxidative stress has been linked to many diseases of aging (diabetes, heart disease, sarcopenia, arthritis, kidney disease)[50], understanding the association between aging and mitochondria is important.

We found nanotunnels, which are thin, double-membrane mitochondrial connections that can transport proteins and nutrients, in all skeletal muscle samples. While healthy humans have almost no nanotunnels [21], we unexpectedly found a moderate number of nanotunnels in young 3-month-old mice (Figures 3E–H), and a consistent increase of nanotunnels in the skeletal muscle of 1-year-old mice. These structures may have an unclear beneficial role in skeletal muscle of mice. Given the association of nanotunnels with human diseases, we predicted that the 2-year-old "aged" mouse skeletal muscle would have the most nanotunnels, however the nanotunnel number was quite heterogeneous in 2-year-old mice and less were observed [12,51]. The 2-year-old samples may have shown fewer nanotunnels due to the high rate of fragmentation (Figure 1) and lack of connectedness (Figure 2) preventing nanotunnel formation. In contrast, perhaps the remaining networks permitted the increased number of nanotunnels in 1-year moderately aged samples. The presence of nanotunnels in the healthy 3-month-old mouse skeletal muscle suggests significant differences in mouse versus human muscle [21].

MICOS proteins play key regulatory roles in mitochondrial structure and function [19,26,37]. We determined by TEM 3D reconstructions that the loss of *Mitofilin*, *CHCHD3*, and *CHCHD6* (Figures 4-5) resulted in fragmentation, disrupted cristae, and smaller mitochondria (Figures 4A–I, Figures 4P–Y; Figure 5), similar to the loss of OPA-1, which is known to cause changes in oxidative phosphorylation (Figures 4Z–AE) [19,23,28]. Overall, mitochondria lacking the MICOS genes had characteristics similar to those of aged mouse skeletal muscle (Figures 1−2). This similarity in phenotype suggests there may be an association. Thus, changes in mitochondrial morphology due to aging may be caused by a lack of MICOS gene expression. This is supported by the RT-qPCR data that showed decreased *CHCHD3*, *CHCHD6*, *Mitofilin*, and *Opa-1* transcription with aging (SFigure 3). Although there is a link between aging and loss of *Opa-1* [24,29], little is known about the role of the MICOS complex in aging. Changes in mitochondrial architecture and loss of integrity may be caused by decreased MICOS proteins; thus, it will be important to develop methods to restore MICOS proteins and *Opa-1* lost during aging to decrease the deleterious effects of mitochondrial dysfunction. Although studies have examined the role of knockouts on mitochondrial dynamics, few studies have examined how loss of MICOS proteins may be restored to mitochondria [23,52].

Many studies have analyzed the mitochondrial metabolome using mouse skeletal muscles [45,53–57]. We found that loss of *Mitofilin* affected cristae morphology (Figures 4G–H), decreased oxidative phosphorylation (Figure 4J), and may have increased lipid and steroid synthesis, which may be important for mitochondrial endoplasmic reticulum contact (MERC) regulation and cristae formation. We found an increase in tryptophan and methyl histidine metabolism (SFigure

4D) and an increase in taurine metabolism and hypotaurine, a key sulfur-containing amino acid for the metabolism of fats. Loss of *Opa-1* also changes amino acid and lipid metabolism, similar to the loss of *Mitofilin* [40–42]. Steroidogenesis, which makes the membrane less rigid, was increased. Since the loss of *Mitofilin*, *CHCHD6*, or *CHCHD3* caused a loss of oxidative capacity (Figure 4J-O; 5K-P), increased steroid synthesis may allow the cell to recover bioenergetic functions, as steroid compounds decrease membrane viscosity, with the incorporation of estrogen [38]. In the absence of *Mitofilin*, the cristae junctions and contact sites fall apart [58]; thus, *Mitofilin* is critical for maintaining cristae [59,60]. Cells lacking *Mitofilin* may make steroids to help the membrane to reconfigure broken cristae. Since the loss of *Opa-1* causes more MERCs [3], loss of *Mitofilin* may increase phospholipids (SFigure 4D) because of increased smooth MERCs, which are associated with lipid changes [61]. This is supported by the fact that biosynthesis of phosphatidylethanolamine and phosphatidylcholine and metabolism of arachidonic acid and sphingolipid increased with loss of *Mitofilin* (SFigure 4D). Since these phospholipids aggregate around MERCs and may shuffle into the ER, *Mitofilin* may be a critical gene for regulating cristae morphology and with a key role in regulating mitochondrial metabolism, which is novel.

Mitofilin may be an important target in the future to restore energy production. Loss of *Mitofilin* may lead to ER stress, which, via ATF4, activates amino acid transporters [62] that further activate mTORC1. ER stress activates mTORC as a result of a decrease in glucose [57]. Critically, mTORC1 affects glucose homeostasis [63], and this may lead to inefficiency in energy use. This can result in changes in autophagy. Therefore, as a downstream effect of *Mitofilin* loss increasing mTORC1, this may explain why deletion of MICOS in *Drosophila* increases autophagy [37]. Similarly, previously loss of *Opa-1* increases ER stress [28], and loss of *Mitofilin* may cause a similar increase in amino acid catabolism. If ER stress activates amino acid transporters, branched-chain amino acids could increase ER stress, resulting in a positive feedback loop that affects the health of the cell, cellular energy, metabolism, and antioxidants. ER stress may also be responsible for the poor performance and fragmentation of mitochondria (Figure 4-5). Loss of *Mitofilin* may result in the breakdown of protein pathways that regulate ER stress. Other amino acid pathways, such as homocysteine (SFigure 4D), are involved in triglyceride uptake and increased intracellular cholesterol, suggesting that proteins like ATF4 [57] and the MICOS complex [15,26] are important for aging. In particular, the MICOS components may prevent mitochondrial fragmentation by blocking ER stress pathways in aging. Further studies are needed to better understand the role of MICOS in MERC formation and the relation between smooth MERC and lipid synthesis.

Although *Mitofilin* is a key component of the MICOS complex, other components are likely also important. The loss of *CHCHD3* or *CHCHD6* leads to a decrease in and disassembly of all *Mitofilin* subcomplex components in mammals, with abnormal cristae morphology and growth defects [33,64–69]. Downregulation of *CHCHD3* is linked to type 2 diabetes [70]. In our metabolomics enrichment dataset (SFigure 5D), loss of *CHCHD3* or *CHCHD6* in mouse myotubes resulted in a preference for alternative fuel sources, such as lactate, lactose, and starches. Supplementation of healthy myotubes with galactose leads to a 30% increase in oxidative capacity (i.e., OCR) due to an increase in AMPK phosphorylation and cytochrome c oxidase (COX) activity, thereby forcing cells to become more oxidative to maintain ATP levels [71]. In our samples, as oxidative metabolism decreased, anaerobic metabolism and lactate levels increased, forcing cells to produce ATP by anaerobic glycolysis. However, long and high-level exposure to D-galactose generates free radicals, which alter MERCs, cause mitochondrial

dysfunction, and induce aging [2,72]. This is the likely explanation for mitochondrial fragmentation in aged samples and loss of the MICOS complex, which should be investigated further.

In conclusion, we present a quantitative evaluation of mitochondrial and cristae morphology in mouse skeletal muscle using 3D reconstructions and TEM analysis. We found oxidative differences upon loss of MICOS proteins. 3D reconstructions of nanotunnels in mitochondria showed novel patterns with a moderate number of nanotunnels in young skeletal mouse tissue and relatively low numbers in the most aged mouse skeletal muscles. Similar changes in mitochondrial morphology were observed in aging muscles and for loss of MICOS proteins in mouse skeletal muscle, and MICOS proteins decreased with age. This suggests a relationship between the MICOS complex and aging, and further studies through 3D reconstruction could elucidate the linkage between age-related muscle dysfunction, the MICOS complex, and disease states in mitochondria.

EXPERIMENTAL PROCEDURES

Animal Care and Maintenance

All procedures for the care of mice were in accordance with humane and ethical protocols approved by the University of Iowa Animal Care and Use Committee (IACUC) following the National Institute of Health (NIH) Guide for the Care and Use of Laboratory Animals as described previously [28]. All experiments used WT male C57Bl/6J mice housed at 22°C on a 12-hour light, 12-hour dark cycle with free access to water and standard chow. Mice were anesthetized with 5% isoflurane/95% oxygen.

RNA Extraction and RT-qPCR

Total RNA was extracted from tissue using TRIzol reagent (Invitrogen, cat #), purified with the RNeasy kit (Qiagen Inc, cat #), and quantitated by the absorbance at 260 nm and 280 nm using a NanoDrop 1000 (NanoDrop products, Wilmington, DE, USA) spectrophotometer. Total RNA (~1 µg) was reverse-transcribed using a High-Capacity cDNA Reverse Transcription Kit (Applied Biosciences, Carlsbad CA, cat #) followed by real-time quantitative PCR (qPCR) reactions using SYBR Green (Life Technologies, Carlsbad, CA, cat #) [73]. Triplicate samples for qPCR (~50 ng) in a 384-well plate were placed into ABI Prism 7900HT instrument (Applied Biosystems) programmed as follows: 1 cycle at 95°C for 10 min; 40 cycles of 95°C for 15 s; 59°C for 15 s, 72°C for 30 s, and 78°C for 10 s; 1 cycle of 95°C for 15 s; 1 cycle of 60°C for 15 s; and one cycle of 95°C for 15 s. Data were normalized to glyceraldehyde-3-phosphate dehydrogenase (*Gapdh*), and results are shown as fold changes. qPCR primers were designed using Primer-Blast or were previously published sequences [28] as shown in Table 1.

Table 1: qPCR Primers Used

Gene	Primers	
Opa-1	Forward	5'-ACCAGGAGACTGTGTCAA-3'
	Reverse	5'-TCTTCAAATAAACGCAGAGGTG-3'
CHCHD3	Forward	5'-GAAAAGAATCCAGGCCCTTCCACGCGC-3'
	Reverse	5'-CAGTGCCTAGCACTTGGCACAACCAGGAA-3'
CHCHD6	Forward	5'-CTCAGCATGGACCTGGTAGGCACTGGGC-3'
	Reverse	5'-GCCTCAATTCCCACATGGAGAAAGTGGC-3'
Mitofilin	Forward	5'-CCTCCGGCAGTGTTCACCTAGTAACCCCTT-3'
	Reverse	5'-TCGCCCGTCGACCTTCAGCACTGAAAACCTAT-3'

Isolation of Satellite Cells

Satellite cell differentiation was performed as previously described [16,28]. Cells were cultured at 37°C, 5% CO_2 Dulbecco's modified Eagle's medium (DMEM; GIBCO, cat #) supplemented with 10% FBS (Atlanta Bio selected, cat #), and 1% penicillin-streptomycin (Gibco, Waltham, MA, USA, cat #).

CRISPR-Cas9 Knockouts

After three days, myotubes were infected with adenovirus to produce the following knockouts—control CRISPR/Cas9 (sc-418922), *CHCHD6* (Mic25) CRISPR (sc-425817), *CHCHD3* (Mic19) CRISPR (sc-425804), and *mitofilin* (Mic60) CRISPR (sc-429376) (Santa Cruz Biotechnology, California, US), with the use of guide RNA (Table 2). We incubated 2.5% relevant CRISPR, 2.5% RNAiMax (ThermoFisher Scientific; cat # 13778075), and 95% Opti-MEM (Gibco; cat #31985070) in a tube for 20 minutes. Cells were washed twice with PBS after removal of the medium and 800 µL of OPT-MEM and 200 µL of the CRISPR mixture were added to each well, ran in triplicates. Cells were incubated for 4 hours at 37 C, 1.0 mL of DMEM medium was added, cells were incubated overnight. The myotubes were then washed with PBS and the medium was replaced. Experiments were performed between 3 and 7 days after infection for a total of 6 days of differentiation.

Table 2: Guide RNA and Plasmids Used

Gene Name	Type of Plasmid	CAS Number
Mitofilin	CRISPR/Cas9 KO (m)	sc-429376
CHCHD6	CRISPR/Cas9 KO (m)	sc-425817
CHCHD3	CRISPR/Cas9 KO (m)	sc-425804
Control	CRISPR/Cas9 KO (m)	sc-418922

Serial Block-Face Scanning Electron Microscope (SBF-SEM) Processing of Mouse Muscle Fibers

SBF-SEM preparation was performed as described previously [17,27,74]. Running on a FEI/Thermo Scientific Volumescope 2 SEM, a state-of-the-art SBF imaging system, we obtained 300−400 ultrathin (0.09 µm) serial sections from the blocks that were processed for conventional TEM. All sections were collected onto formvar-coated slot grids (Pella, Redding CA), stained, and imaged as previously described [17,27,74].

Quantification of TEM Micrographs and Parameters Using ImageJ

Quantification of TEM images was performed as described previously using the NIH *ImageJ* software [16,27]. Cells were divided into four quadrants and two quadrants were selected randomly for complete analysis. From each individual, a minimum of 10 cells were measured with three analyses to obtain accurate and reproducible values. If variability occurred, the number of cells was expanded to 30 cells per individual to reduce the variability.

Segmentation and Quantification of 3D SBF-SEM Images Using Amira

Intermyofibrillar (IMF) mitochondria are located between myofibrils, arranged in pairs at the z-band of each sarcomere, with 2D elongated tubular shapes [75]. However, it is not known how aging affects mitochondrial orientation, the structure of C-band sarcomeres, or the morphological changes in incomplete fission known as nanotunnels. For each region of interest across the three age groups, we analyzed 300 slices at 50 µm intervals at the transverse intervals.

For 3D reconstruction, SBF-SEM images were manually segmented in Amira as described previously [17,27]. All serial sections (300−400 slices) were loaded onto Amira and structural features were traced manually on sequential slices of micrograph blocks. Structures in mice were collected from 30–50 serial sections that were then stacked, aligned, and visualized using Amira to make videos and quantify volumetric structures. An average of 500 total mitochondria across four ROIs from 3 mice were collected for quantification. For 3D reconstruction of myotubes, approximately 20 mitochondria from a minimum of 10 cells were collected. Quantification of SBF-SEM images was performed as described previously [17] using the Amira software (Thermo Scientific).

Data Analysis

All SBF-SEM and TEM data were presented as the mean of at least three independent experiments with similar outcomes. Results were presented as mean ± standard error with individual data points shown. Data with only two groups were analyzed using an unpaired, t-test. For nanotunnel quantification, a Mann-Whitney test (unpaired, nonparametric) t-test was performed between two groups. If more than two groups were compared, one-way ANOVA was performed, and significance was assessed using Fisher's protected least significant difference (LSD) test. GraphPad Prism software package was used for t-tests and ANOVA analyses (La Jolla, CA, USA). For all statistical analyses, $p < 0.05$ indicated a significant difference. Higher degrees of statistical significance (**, ***, ****) were defined as $p < 0.01$, $p < 0.001$, and $p < 0.0001$, respectively.

Gas Chromatography-Mass Spectrometry (GC-MS)

Samples were extracted for metabolites and prepared as previously designed[76]. The profiling of the metabolites was performed using TraceFinder 4.1 with standard verified peaks and retention times. TraceFinder was used to compare metabolite peaks in each sample against an in-house library of standards. TraceFinder was also used for GC-MS peak integration to obtain peak areas for each metabolite. After this analysis, we used previously described protocols [77] to correct for drift over time by using QC samples run at both the beginning and end of the sequence. The data was then normalized to an internal standard to control for extraction, derivatization, and/or loading effects.

Liquid Chromatography-Mass Spectrometry (LC-MS)

LC-MS was performed for myotubes as previously described[76]. TraceFinder 4.1 software was used for analysis and metabolites were identified based on an in-house library. Drift was corrected for as described above [77]. Data were normalized and further visualization and analysis were performed on MetaboAnalyst 5.0 [78].

Analyzing Metabolomic Data

Metabolomic analysis was performed as described previously [76] using the web service MetaboAnalyst 5.0 (https://www.metaboanalyst.ca/MetaboAnalyst/ModuleView.xhtml, last accessed on 8 February 2022) that combines machine learning methods and statistics to group data using PCA, heat mapping, metabolite set enrichment analysis, and statistical analysis. One-way ANOVA and Fisher's LSD multiple comparison test were also used. PCA uses score plots to provide an overview of variance for the principal components. Heatmaps separate hierarchical clusters leading to progressively larger clusters. Clusters are based on similarity using Euclidean

distance and Ward's linkage to minimize the clustering needed. Metabolite Set Enrichment Analysis (MSEA), which determines whether a set of functionally related metabolites is altered, can be used to identify consistent changes across many metabolites with similar roles. Overrepresentation analysis determines whether a group of compounds is overrepresented in comparison to pure chance and whether a group of metabolites have similar changes. In this analysis, the fold enrichment was calculated by dividing the observed hits by the expected metabolites. Expected number of hits are calculated by MetaboAnalyst 5.0. GraphPad Prism software (La Jolla, CA, USA) was used for statistical analysis with data expressed as mean ± standard deviation, and one-tailed p-values ≤ 0.01 were considered significant.

Measurement of OCR Using Seahorse

Using an XF24 extracellular flux (XF) bioanalyzer (Agilent Technologies/Seahorse Bioscience, North Billerica, MA, USA), OCR was measured for *Opa-1*, *CHCHD3*, *CHCHD6*, or *Mitofilin* knocked down cells as previously described[28]. Three independent experiments were performed with four to six replicates for each time and for each condition and representative data from the replicates are shown.

ACKNOWLEDGEMENTS

We would like to thank Melanie McReynolds for her advice on processing metabolomic samples and Mariya Sweetwyne for her advice as an aging expert. This work was supported by UNCF/BMS EE United Negro College Fund/Bristol-Myers Squibb E.E. T-32, number DK007563 entitled Multidisciplinary Training in Molecular Endocrinology to Z.V.; Just Postgraduate Fellowship in the Life Sciences Fellowship to H.K.B.; NSF MCB #2011577I to S.A.M.; The UNCF/BMS E.E. Just Faculty Fund, Burroughs Wellcome Fund Career Awards at the Scientific Interface Award, Burroughs Wellcome Fund Ad-hoc Award, NIH Small Research Pilot Subaward to 5R25HL106365-12 from the NIH PRIDE Program, DK020593, Vanderbilt Diabetes and Research Training Center for DRTC Alzheimer's Disease Pilot & Feasibility Program to A.H.J. Its contents are solely the responsibility of the authors and do not necessarily represent the official view of the NIH. The funders had no role in study design, data collection and analysis, decision to publish, or preparation of the manuscript.

CONFLICT OF INTEREST

The authors declare that they have no conflict of interest.

CONSENT FOR PUBLICATION

All authors have agreed to the final version of this manuscript.

DATA AVAILABILITY STATEMENT

The data that support the findings of this study are available from the corresponding author upon reasonable request.

AUTHOR CONTRIBUTIONS

Z.V., E.G., L.V., J.S., H.K.B., S.A.M., M.A.P., A.H.J., J.A.G., and D.D. conceived and designed research; A.G.M., A.C., L.V., Z.V., T.A.C, B.C.M., J.L., H.K.B., B.R, C.E., D.D., A.H.J., and

J.A.G. performed experiments; J.D., K.N, J.S., E.G., Z.V., J.L., B.R., T.A.C., A.K.R., A.M.Q., V.E., E.G., D.D., , J.A.G., and A.H.J. analyzed data; B.T, K.N, J.S., E.G., Z.V., S.A.M., A.M.Q., V.E., H.K.B., A.C., A.G.M., J.D., M.A.P., D.D., J.A.G., and A.H.J.. interpreted results of experiments and prepared figures; K.N, E.G., Z.V., J.S., S.A.M., L.V., A.G.M., M.A.P., A.K.R., B.C.M., B.T., C.E., A.C., H.K.B., D.D., J.A.G., and A.H.J. drafted manuscript, edited, and revised manuscript; A.H.J., D.D., and J.A.G. approved final version of manuscript.

REFERENCES

1. Bratic A, Larsson N-G. The role of mitochondria in aging. *The Journal of clinical investigation*. 2013;123:951–957.

2. Barja G. The mitochondrial free radical theory of aging. *Progress in molecular biology and translational science*. 2014;127:1–27.

3. Rowland AA, Voeltz GK. Endoplasmic reticulum–mitochondria contacts: function of the junction. *Nature reviews Molecular cell biology*. 2012;13:607–615.

4. Dai D-F, Santana LF, Vermulst M, Tomazela DM, Emond MJ, MacCoss MJ, Gollahon K, Martin GM, Loeb LA, Ladiges WC, Rabinovitch PS. Overexpression of catalase targeted to mitochondria attenuates murine cardiac aging. *Circulation*. 2009;119:2789–2797.

5. Xu H, Ranjit R, Richardson A, Van Remmen H. Muscle mitochondrial catalase expression prevents neuromuscular junction disruption, atrophy, and weakness in a mouse model of accelerated sarcopenia. *J Cachexia Sarcopenia Muscle*. 2021;12:1582–1596.

6. Friederich M, Hansell P, Palm F. Diabetes, oxidative stress, nitric oxide and mitochondria function. *Current diabetes reviews*. 2009;5:120–144.

7. Renken CW. The structure of mitochondria. 2004.

8. Cogliati S, Enriquez JA, Scorrano L. Mitochondrial cristae: where beauty meets functionality. *Trends in biochemical sciences*. 2016;41:261–273.

9. Kühlbrandt W. Structure and function of mitochondrial membrane protein complexes. *BMC biology*. 2015;13:1–11.

10. Otera H, Ishihara N, Mihara K. New insights into the function and regulation of mitochondrial fission. *Biochimica et Biophysica Acta (BBA)-Molecular Cell Research*. 2013;1833:1256–1268.

595 11. Favaro G, Romanello V, Varanita T, Desbats MA, Morbidoni V, Tezze C, Albiero M,
596 Canato M, Gherardi G, De Stefani D. DRP1-mediated mitochondrial shape controls calcium
597 homeostasis and muscle mass. *Nature communications*. 2019;10:1–17.

598 12. Vincent AE, Turnbull DM, Eisner V, Hajnóczky G, Picard M. Mitochondrial Nanotunnels.
599 *Trends Cell Biol*. 2017;27:787–799.

600 13. Zhang L, Trushin S, Christensen TA, Bachmeier BV, Gateno B, Schroeder A, Yao J, Itoh K,
601 Sesaki H, Poon WW. Altered brain energetics induces mitochondrial fission arrest in
602 Alzheimer's Disease. *Scientific reports*. 2016;6:1–12.

603 14. Zhang J, He Z, Fedorova J, Logan C, Bates L, Davitt K, Le V, Murphy J, Li M, Wang M,
604 Lakatta EG, Ren D, Li J. Alterations in mitochondrial dynamics with age-related
605 Sirtuin1/Sirtuin3 deficiency impair cardiomyocyte contractility. *Aging Cell*. 2021;20:e13419.

606 15. Kozjak-Pavlovic V. The MICOS complex of human mitochondria. *Cell and tissue research*.
607 2017;367:83–93.

608 16. Lam J, Katti P, Biete M, Mungai M, AshShareef S, Neikirk K, Lopez EG, Vue Z,
609 Christensen TA, Beasley HK. A Universal Approach to Analyzing Transmission Electron
610 Microscopy with ImageJ. *bioRxiv*. 2021.

611 17. Garza-Lopez E, Vue Z, Katti P, Neikirk K, Biete M, Lam J, Beasley HK, Marshall AG,
612 Rodman TA, Christensen TA, Salisbury JL, Vang L, Mungai M, AshShareef S, Murray SA,
613 Shao J, Streeter J, Glancy B, Pereira RO, Abel ED, Hinton A. Protocols for Generating
614 Surfaces and Measuring 3D Organelle Morphology Using Amira. *Cells*. 2022;11:65.

615 18. Rampelt H, Zerbes RM, van der Laan M, Pfanner N. Role of the mitochondrial contact site
616 and cristae organizing system in membrane architecture and dynamics. *Biochimica et*
617 *Biophysica Acta (BBA)-Molecular Cell Research*. 2017;1864:737–746.

618 19. Hu C, Shu L, Huang X, Yu J, Gong L, Yang M, Wu Z, Gao Z, Zhao Y, Chen L. OPA1 and
619 MICOS Regulate mitochondrial crista dynamics and formation. *Cell death & disease*.
620 2020;11:1–17.

621 20. Friedman JR, Mourier A, Yamada J, McCaffery JM, Nunnari J. MICOS coordinates with
622 respiratory complexes and lipids to establish mitochondrial inner membrane architecture.
623 *Elife*. 2015;4:e07739.

624 21. Vincent AE, White K, Davey T, Philips J, Ogden RT, Lawless C, Warren C, Hall MG, Ng
625 YS, Falkous G. Quantitative 3D mapping of the human skeletal muscle mitochondrial
626 network. *Cell reports*. 2019;26:996–1009.

627 22. Koopman WJH, Visch H-J, Verkaart S, van den Heuvel LWPJ, Smeitink JAM, Willems
628 PHGM. Mitochondrial network complexity and pathological decrease in complex I activity
629 are tightly correlated in isolated human complex I deficiency. *Am J Physiol Cell Physiol*.
630 2005;289:C881-890.

631 23. Zheng J, Croteau DL, Bohr VA, Akbari M. Diminished OPA1 expression and impaired
632 mitochondrial morphology and homeostasis in Aprataxin-deficient cells. *Nucleic acids*
633 *research*. 2019;47:4086–4110.

634 24. Varanita T, Soriano ME, Romanello V, Zaglia T, Quintana-Cabrera R, Semenzato M,
635 Menabò R, Costa V, Civiletto G, Pesce P. The OPA1-dependent mitochondrial cristae
636 remodeling pathway controls atrophic, apoptotic, and ischemic tissue damage. *Cell*
637 *metabolism*. 2015;21:834–844.

638 25. Khin PP, Hong Y, Yeon M, Lee DH, Lee JH, Jun H-S. Dulaglutide improves muscle
639 function by attenuating inflammation through OPA-1-TLR-9 signaling in aged mice. *Aging*
640 *(Albany NY)*. 2021;13:21962–21974.

641 26. Li H, Ruan Y, Zhang K, Jian F, Hu C, Miao L, Gong L, Sun L, Zhang X, Chen S.
642 Mic60/Mitofilin determines MICOS assembly essential for mitochondrial dynamics and
643 mtDNA nucleoid organization. *Cell Death & Differentiation*. 2016;23:380–392.

644 27. Hinton A, Katti P, Christensen TA, Mungai M, Shao J, Zhang L, Trushin S, Alghanem A,
645 Jaspersen A, Geroux RE. A comprehensive approach for artifact-free sample preparation and
646 assessment of mitochondrial morphology in tissue and cultured cells. *bioRxiv*. 2021.

647 28. Pereira RO, Tadinada SM, Zasadny FM, Oliveira KJ, Pires KMP, Olvera A, Jeffers J,
648 Souvenir R, Mcglauflin R, Seei A. OPA 1 deficiency promotes secretion of FGF 21 from
649 muscle that prevents obesity and insulin resistance. *The EMBO journal*. 2017;36:2126–2145.

650 29. Tezze C, Romanello V, Desbats MA, Fadini GP, Albiero M, Favaro G, Ciciliot S, Soriano
651 ME, Morbidoni V, Cerqua C, Loefler S, Kern H, Franceschi C, Salvioli S, Conte M, Blaauw
652 B, Zampieri S, Salviati L, Scorrano L, Sandri M. Age-Associated Loss of OPA1 in Muscle
653 Impacts Muscle Mass, Metabolic Homeostasis, Systemic Inflammation, and Epithelial
654 Senescence. *Cell Metab*. 2017;25:1374-1389.e6.

655 30. John GB, Shang Y, Li L, Renken C, Mannella CA, Selker JM, Rangell L, Bennett MJ, Zha J.
656 The mitochondrial inner membrane protein mitofilin controls cristae morphology. *Molecular*
657 *biology of the cell*. 2005;16:1543–1554.

658 31. Ding C, Wu Z, Huang L, Wang Y, Xue J, Chen S, Deng Z, Wang L, Song Z, Chen S.
659 Mitofilin and CHCHD6 physically interact with Sam50 to sustain cristae structure. *Scientific*
660 *reports*. 2015;5:1–11.

661 32. Darshi M, Taylor SS. Mitochondrial ChChD3 acts as a Scaffold for Mitofilin, Sam50 and
662 PKA. 2008.

663 33. An J, Shi J, He Q, Lui K, Liu Y, Huang Y, Sheikh MS. CHCM1/CHCHD6, novel
664 mitochondrial protein linked to regulation of mitofilin and mitochondrial cristae
665 morphology. *Journal of Biological Chemistry*. 2012;287:7411–7426.

34. Ott C, Dorsch E, Fraunholz M, Straub S, Kozjak-Pavlovic V. Detailed analysis of the human mitochondrial contact site complex indicate a hierarchy of subunits. *PloS one*. 2015;10:e0120213.

35. Kondadi AK, Anand R, Reichert AS. Functional interplay between cristae biogenesis, mitochondrial dynamics and mitochondrial DNA integrity. *International journal of molecular sciences*. 2019;20:4311.

36. Stephan T, Brüser C, Deckers M, Steyer AM, Balzarotti F, Barbot M, Behr TS, Heim G, Hübner W, Ilgen P. MICOS assembly controls mitochondrial inner membrane remodeling and crista junction redistribution to mediate cristae formation. *The EMBO journal*. 2020;39:e104105.

37. Wang L, Hsu T, Lin H, Fu C. Drosophila MICOS knockdown impairs mitochondrial structure and function and promotes mitophagy in muscle tissue. *Biology Open*. 2020;9:bio054262.

38. Torres MJ, Kew KA, Ryan TE, Pennington ER, Lin C-T, Buddo KA, Fix AM, Smith CA, Gilliam LA, Karvinen S, Lowe DA, Spangenburg EE, Zeczycki TN, Shaikh SR, Neufer PD. 17β-Estradiol Directly Lowers Mitochondrial Membrane Microviscosity and Improves Bioenergetic Function in Skeletal Muscle. *Cell Metabolism*. 2018;27:167-179.e7.

39. Kitajima Y, Ono Y. Estrogens maintain skeletal muscle and satellite cell functions. *Journal of Endocrinology*. 2016;229:267–275.

40. Wasilewski M, Semenzato M, Rafelski SM, Robbins J, Bakardjiev AI, Scorrano L. Optic Atrophy 1-Dependent Mitochondrial Remodeling Controls Steroidogenesis in Trophoblasts. *Current Biology*. 2012;22:1228–1234.

41. Sarzi E, Seveno M, Angebault C, Milea D, Rönnbäck C, Quilès M, Adrian M, Grenier J, Caignard A, Lacroux A, Lavergne C, Reynier P, Larsen M, Hamel CP, Delettre C, Lenaers G, Müller A. Increased steroidogenesis promotes early-onset and severe vision loss in females with OPA1 dominant optic atrophy. *Human Molecular Genetics*. 2016;25:2539–2551.

42. Chao de la Barca JM, Fogazza M, Rugolo M, Chupin S, Del Dotto V, Ghelli AM, Carelli V, Simard G, Procaccio V, Bonneau D, Lenaers G, Reynier P, Zanna C. Metabolomics hallmarks OPA1 variants correlating with their in vitro phenotype and predicting clinical severity. *Hum Mol Genet*. 2020;29:1319–1329.

43. Dahl R, Larsen S, Dohlmann TL, Qvortrup K, Helge JW, Dela F, Prats C. Three-dimensional reconstruction of the human skeletal muscle mitochondrial network as a tool to assess mitochondrial content and structural organization. *Acta Physiol (Oxf)*. 2015;213:145–155.

44. Glancy B, Hartnell LM, Malide D, Yu Z-X, Combs CA, Connelly PS, Subramaniam S, Balaban RS. Mitochondrial reticulum for cellular energy distribution in muscle. *Nature*. 2015;523:617–620.

703 45. Garnier A, Fortin D, Delomenie C, Momken I, Veksler V, Ventura-Clapier R. Depressed
704 mitochondrial transcription factors and oxidative capacity in rat failing cardiac and skeletal
705 muscles. *The Journal of physiology*. 2003;551:491–501.

706 46. Mukund K, Subramaniam S. Skeletal muscle: A review of molecular structure and function,
707 in health and disease. *Wiley Interdisciplinary Reviews: Systems Biology and Medicine*.
708 2020;12:e1462.

709 47. Lin I-H, Chang J-L, Hua K, Huang W-C, Hsu M-T, Chen Y-F. Skeletal muscle in aged mice
710 reveals extensive transformation of muscle gene expression. *BMC genetics*. 2018;19:1–13.

711 48. Galpin AJ, Raue U, Jemiolo B, Trappe TA, Harber MP, Minchev K, Trappe S. Human
712 skeletal muscle fiber type specific protein content. *Anal Biochem*. 2012;425:175–182.

713 49. Sanz A, Stefanatos RK. The mitochondrial free radical theory of aging: a critical view.
714 *Current aging science*. 2008;1:10–21.

715 50. Rolo AP, Palmeira CM. Diabetes and mitochondrial function: role of hyperglycemia and
716 oxidative stress. *Toxicology and applied pharmacology*. 2006;212:167–178.

717 51. Lavorato M, Iyer VR, Dewight W, Cupo RR, Debattisti V, Gomez L, Fuente SD la, Zhao Y-
718 T, Valdivia HH, Hajnóczky G, Franzini-Armstrong C. Increased mitochondrial
719 nanotunneling activity, induced by calcium imbalance, affects intermitochondrial matrix
720 exchanges. *PNAS*. 2017;114:E849–E858.

721 52. Liu T, Woo JA, Bukhari MZ, LePochat P, Chacko A, Selenica MB, Yan Y, Kotsiviras P,
722 Buosi SC, Zhao X. CHCHD10-regulated OPA1-mitofilin complex mediates TDP-43-
723 induced mitochondrial phenotypes associated with frontotemporal dementia. *The FASEB*
724 *Journal*. 2020;34:8493–8509.

725 53. de La Barca JMC, Arrázola MS, Bocca C, Arnauné-Pelloquin L, Iuliano O, Tcherkez G,
726 Lenaers G, Simard G, Belenguer P, Reynier P. The metabolomic signature of Opa1
727 deficiency in rat primary cortical neurons shows aspartate/glutamate depletion and
728 phospholipids remodeling. *Scientific reports*. 2019;9:1–8.

729 54. Bocca C, Nzoughet JK, Leruez S, Amati-Bonneau P, Ferré M, Kane M-S, Veyrat-Durebex
730 C, de La Barca JMC, Chevrollier A, Homedan C. A plasma metabolomic signature involving
731 purine metabolism in human optic atrophy 1 (OPA1)-related disorders. *Investigative*
732 *ophthalmology & visual science*. 2018;59:185–195.

733 55. de La Barca JMC, Simard G, Sarzi E, Chaumette T, Rousseau G, Chupin S, Gadras C,
734 Tessier L, Ferré M, Chevrollier A. Targeted metabolomics reveals early dominant optic
735 atrophy signature in optic nerves of Opa1delTTAG/+ mice. *Investigative ophthalmology &*
736 *visual science*. 2017;58:812–820.

737 56. Garcia-Cazarin ML, Snider NN, Andrade FH. Mitochondrial isolation from skeletal muscle.
738 *JoVE (Journal of Visualized Experiments)*. 2011;:e2452.

739 57. Wortel IMN, van der Meer LT, Kilberg MS, van Leeuwen FN. Surviving Stress: Modulation
740 of ATF4-Mediated Stress Responses in Normal and Malignant Cells. *Trends Endocrinol*
741 *Metab*. 2017;28:794–806.

742 58. Cristae undergo continuous cycles of membrane remodelling in a MICOS-dependent
743 manner. *EMBO reports*. 2020;21:e49776.

744 59. Hessenberger M, Zerbes RM, Rampelt H, Kunz S, Xavier AH, Purfürst B, Lilie H, Pfanner
745 N, van der Laan M, Daumke O. Regulated membrane remodeling by Mic60 controls
746 formation of mitochondrial crista junctions. *Nat Commun*. 2017;8:15258.

747 60. Tarasenko D, Barbot M, Jans DC, Kroppen B, Sadowski B, Heim G, Möbius W, Jakobs S,
748 Meinecke M. The MICOS component Mic60 displays a conserved membrane-bending
749 activity that is necessary for normal cristae morphology. *J Cell Biol*. 2017;216:889–899.

750 61. Rieusset J. The role of endoplasmic reticulum-mitochondria contact sites in the control of
751 glucose homeostasis: an update. *Cell death & disease*. 2018;9:1–12.

752 62. Han J, Back SH, Hur J, Lin Y-H, Gildersleeve R, Shan J, Yuan CL, Krokowski D, Wang S,
753 Hatzoglou M. ER-stress-induced transcriptional regulation increases protein synthesis
754 leading to cell death. *Nature cell biology*. 2013;15:481–490.

755 63. Zhang X, Wang X, Yuan Z, Radford SJ, Liu C, Libutti SK, Zheng XFS. Amino acids-
756 Rab1A-mTORC1 signaling controls whole-body glucose homeostasis. *Cell Reports*.
757 2021;34:108830.

758 64. Darshi M, Mendiola VL, Mackey MR, Murphy AN, Koller A, Perkins GA, Ellisman MH,
759 Taylor SS. ChChd3, an inner mitochondrial membrane protein, is essential for maintaining
760 crista integrity and mitochondrial function. *Journal of biological chemistry*. 2011;286:2918–
761 2932.

762 65. Piñero-Martos E, Ortega-Vila B, Pol-Fuster J, Cisneros-Barroso E, Ruiz-Guerra L, Medina-
763 Dols A, Heine-Suñer D, Lladó J, Olmos G, Vives-Bauzà C. Disrupted in schizophrenia 1
764 (DISC1) is a constituent of the mammalian mitochondrial contact site and cristae organizing
765 system (MICOS) complex, and is essential for oxidative phosphorylation. *Human Molecular*
766 *Genetics*. 2016;25:4157–4169.

767 66. Genin EC, Plutino M, Bannwarth S, Villa E, Cisneros-Barroso E, Roy M, Ortega-Vila B,
768 Fragaki K, Lespinasse F, Pinero-Martos E. CHCHD 10 mutations promote loss of
769 mitochondrial cristae junctions with impaired mitochondrial genome maintenance and
770 inhibition of apoptosis. *EMBO molecular medicine*. 2016;8:58–72.

771 67. Park Y-U, Jeong J, Lee H, Mun JY, Kim J-H, Lee JS, Nguyen MD, Han SS, Suh P-G, Park
772 SK. Disrupted-in-schizophrenia 1 (DISC1) plays essential roles in mitochondria in
773 collaboration with Mitofilin. *Proceedings of the National Academy of Sciences*.
774 2010;107:17785–17790.

775 68. Genin EC, Bannwarth S, Lespinasse F, Ortega-Vila B, Fragaki K, Itoh K, Villa E, Lacas-
776 Gervais S, Jokela M, Auranen M, Ylikallio E, Mauri-Crouzet A, Tyynismaa H, Vihola A,
777 Augé G, Cochaud C, Sesaki H, Ricci J-E, Udd B, Vives-Bauza C, Paquis-Flucklinger V.
778 Loss of MICOS complex integrity and mitochondrial damage, but not TDP-43 mitochondrial
779 localisation, are likely associated with severity of CHCHD10-related diseases. *Neurobiology*
780 *of Disease*. 2018;119:159–171.

781 69. Bannwarth S, Ait-El-Mkadem S, Chaussenot A, Genin EC, Lacas-Gervais S, Fragaki K,
782 Berg-Alonso L, Kageyama Y, Serre V, Moore DG, Verschueren A, Rouzier C, Le Ber I,
783 Augé G, Cochaud C, Lespinasse F, N'Guyen K, de Septenville A, Brice A, Yu-Wai-Man P,
784 Sesaki H, Pouget J, Paquis-Flucklinger V. A mitochondrial origin for frontotemporal
785 dementia and amyotrophic lateral sclerosis through CHCHD10 involvement. *Brain*.
786 2014;137:2329–2345.

787 70. Eramo MJ, Lisnyak V, Formosa LE, Ryan MT. The 'mitochondrial contact site and cristae
788 organising system' (MICOS) in health and human disease. *The Journal of Biochemistry*.
789 2020;167:243–255.

790 71. Martin CR, Preedy VR, Rajendram R. Assessments, Treatments and Modeling in Aging and
791 Neurological Disease: The Neuroscience of Aging. Academic Press; 2021: 1-608.

792 72. Kandlur A, Satyamoorthy K, Gangadharan G. Oxidative Stress in Cognitive and Epigenetic
793 Aging: A Retrospective Glance. *Frontiers in Molecular Neuroscience*. 2020;13. Available at
794 https://www.frontiersin.org/article/10.3389/fnmol.2020.00041. Accessed March 17, 2022.

795 73. Boudina S, Sena S, Theobald H, Sheng X, Wright JJ, Hu XX, Aziz S, Johnson JI, Bugger H,
796 Zaha VG, Abel ED. Mitochondrial energetics in the heart in obesity-related diabetes: direct
797 evidence for increased uncoupled respiration and activation of uncoupling proteins.
798 *Diabetes*. 2007;56:2457–2466.

799 74. Neikirk K, Vue Z, Katti P, Shao J, Christensen TA, Lopez EG, Marshall A, Palavicino-
800 Maggio C, Ponce J, Alghanem A. Systematic Transmission Electron Microscopy-Based
801 Identification of Cellular Degradation Machinery. *bioRxiv*. 2021.

802 75. Vendelin M, Béraud N, Guerrero K, Andrienko T, Kuznetsov AV, Olivares J, Kay L, Saks
803 VA. Mitochondrial regular arrangement in muscle cells: a "crystal-like" pattern. *American*
804 *Journal of Physiology-Cell Physiology*. 2005;288:C757–C767.

805 76. Phillips MA, Arnold KR, Vue Z, Beasley HK, Garza-Lopez E, Marshall AG, Morton DJ,
806 McReynolds MR, Barter TT, Hinton A. Combining Metabolomics and Experimental
807 Evolution Reveals Key Mechanisms Underlying Longevity Differences in Laboratory
808 Evolved Drosophila melanogaster Populations. *International Journal of Molecular Sciences*.
809 2022;23:1067.

810 77. Li B, Tang J, Yang Q, Li S, Cui X, Li Y, Chen Y, Xue W, Li X, Zhu F. NOREVA:
811 normalization and evaluation of MS-based metabolomics data. *Nucleic acids research*.
812 2017;45:W162–W170.

78. Chong J, Soufan O, Li C, Caraus I, Li S, Bourque G, Wishart DS, Xia J. MetaboAnalyst 4.0: towards more transparent and integrative metabolomics analysis. *Nucleic acids research*. 2018;46:W486–W494.

(13) **SUPPORTING INFORMATION**

(14) TABLES

(15) FIGURE LEGEND

Figure 1: Decreased mitochondrial size and volume in skeletal muscle of aged mice in SBF-SEM 3D reconstructions.
(**A-C**) Representative SBF-SEM orthoslice for skeletal muscle. (**A'-C'**) 3D reconstructions of mitochondria (various colors) in skeletal muscle mouse tissues of different ages overlaid on ortho slices. (**A''-C''**) 3D reconstructed and isolated mitochondria for clear visualization. (**A'-C''**) Pseudo-colored individual mitochondria in skeletal muscle to differentiate micro-level changes. (**A, A', A''**) The 2D ortho slice, the overlay of the 2D ortho slice, and the 3D reconstruction with individually colored mitochondria in tissue from 3-month-old mice. (**B, B', B''**) The 2D ortho slice, the overlay of the 2D ortho slice, and the 3D reconstruction with individually colored mitochondria in tissue from 1-year-old mice. (**C, C', C''**) The 2D ortho slice, the overlay of the 2D ortho slice, and the 3D reconstruction with individually colored mitochondria in tissue from 2-year-old mice. (**D-F**) Quantification of 3D reconstructions, with each dot representing the overall average of all mitochondria quantified for each mouse. (**D**) Mitochondrial volume in skeletal muscle of different ages. (**E-F**) Mitochondrial area and perimeter in skeletal tissues of different ages. Significance values * $p \leq 0.05$, **** $p \leq 0.0001$.

Figure 2: SBF-SEM 3D reconstruction in skeletal muscle of aged mice.
(**A-C**) 3D reconstruction of individually colored mitochondria from a transverse view for mouse skeletal tissues of different ages. (**A'-C'**) 3D reconstruction of individually colored mitochondria from a longitudinal view in skeletal muscle tissues of different ages. (**D**) MBI for mitochondria in tissues of different ages, with each dot representing the overall average mitochondria quantified for each of the three mouses. (**F**) Sphericity of mitochondria in skeletal muscle of different ages, with dots representing the average of all mitochondria quantified for each of the three mouses. (**E**) Representative examples of 3D reconstruction of mitochondria in skeletal muscle of different ages organized by volume. Significance values **** $p \leq 0.0001$.

Figure 3. Mitochondrial nanotunnels in skeletal mouse tissue.
(**A-C**) TEM tracing showing identified nanotunnels across aged cohorts in skeletal mouse tissue. (**D**) Representative examples of 3D reconstruction of nanotunnels in tissues of different ages organized by volume. (**E-H**) Quantification comparing frequency, average nanotunnel amount, nanotunnel length, and diameter of nanotunnels, respectively, across aged cohorts. (**I**) Histogram showing frequency of various nanotunnel lengths for each age group. (**J**) Histogram showing frequency of various nanotunnel diameters for each age group. ** $p \leq 0.01$, **** $p \leq 0.0001$.

Figure 4. Knockout of *Mitofilin* or *Opa-1* in myotubes results in changes in mitochondria, cristae, and oxygen consumption rates.
(**A-C**) Representative images of mitochondria and cristae from myotubes of OPA-1 and *Mitofilin* knockout mice compared to WT. (**D**) Mitochondrial area in myotubes of *Opa-1*, and *Mitofilin* knockout mice compared to WT. (**E**) Circularity index, measuring the roundness and symmetry of mitochondria, in myotubes of *Opa-1* and *Mitofilin* knockout mice compared to WT. (**F**) The

number of mitochondria in myotubes of *Opa-1* and *Mitofilin* knockout mice compared to WT. (**G**) Quantification of individual cristae in myotubes of *Opa-1* and *Mitofilin* knockout mice compared to WT. (**H**) Cristae scores measuring the uniformity and idealness of cristae in myotubes of *Opa-1* and *Mitofilin* knockout mice compared to WT. (**I**) Surface area of the average cristae in myotubes of *Opa-1* and *Mitofilin* knockout mice compared to WT. (**J**) OCR in myotubes of *Opa-1* and *Mitofilin* knockout mice compared to WT. (**K**) Basal OCR, the net respiration rate once non-mitochondrial respiration has been removed, in myotubes of *Opa-1*, and *Mitofilin* knockout mice compared to WT. (**L**) ATP-linked respiration, shown from intervals 4−7 in the OCR graphs, was determined by the addition of oligomycin (an inhibitor of respiration), thus representing the respiration dependent on ATP, in myotubes of *Opa-1* and *Mitofilin* knockout mice compared to WT. (**M**) Maximum OCR, represented by the peak from intervals 7−11 once non-mitochondrial respiration was deducted, in myotubes of *Opa-1* and *Mitofilin* knockout mice compared to WT. (**N**) The reserve capacity, which is represented by the difference between basal OCR and maximum OCR, in myotubes of *Opa-1* and *Mitofilin* knockout mice compared to WT. (**O**) Proton leak, representing non-phosphorylating electron transfer, in myotubes of *Opa-1* and *Mitofilin* knockout mice compared to WT. Significance values ** $p \leq 0.01$, *** $p \leq 0.001$, **** $p \leq 0.0001$.

Figure 5. Knockout of MICOS complex proteins in myotubes results in changes in mitochondria, cristae, and oxygen consumption rates.
(**A-D**) Representative images of mitochondria and cristae from myotubes of *Opa-1*, *CHCHD3*, and *CHCHD6* knockout mice compared to WT. (**E**) Mitochondrial area in myotubes of *CHCHD3*, *CHCHD6*, and *Opa-1* knockout mice compared to WT. (**F**) Circularity index in myotubes of *CHCHD3*, *CHCHD6*, and *Opa-1* knockout mice compared to WT. (**G**) Mitochondria in myotubes of *CHCHD3*, *CHCHD6*, and *Opa-1* knockout mice compared to WT. (**H**) Quantification of individual cristae in myotubes of *CHCHD3*, *CHCHD6*, and *Opa-1* knockout mice compared to WT. (**I**) Cristae score in myotubes of *CHCHD3*, *CHCHD6*, and *Opa-1* knockout mice compared to WT. (**J**) Surface area of the average cristae in myotubes of *CHCHD3*, *CHCHD6*, and *Opa-1* knockout mice compared to WT. (**K**) OCR in myotubes of *CHCHD3, CHCHD6*, and *Opa-1* knockout mice compared to WT. **(L)** Basal OCR in myotubes of *CHCHD3*, *CHCHD6*, and *Opa-1* knockout mice compared to WT. (**M**) ATP-linked respiration in myotubes of *CHCHD3*, *CHCHD6*, and *Opa-1* knockout mice compared to WT. (**N**) Maximum OCR in myotubes of *CHCHD3*, *CHCHD6*, and *Opa-1* knockout mice compared to WT. (**O**) The reserve capacity in myotubes of *CHCHD3*, *CHCHD6*, and *Opa-1* knockout mice compared to WT. (**P**) Proton leak in myotubes of *Opa-1*, *CHCHD3*, and *CHCHD6*, knockout mice compared to WT. Significance values * $p \leq 0.05$, ** $p \leq 0.01$, *** $p \leq 0.001$, **** $p \leq 0.0001$.

Figure 6. Loss of OPA-1 or MICOS complex proteins in myotubes decreases mitochondrial size and length.
(**A-E**) Representative images showing 3D reconstructions of mitochondria in myotubes of *Opa-1*, *Mitofilin CHCHD3*, and *CHCHD6* knockout mice compared to WT. (**F**) Mitochondrial 3D length in myotubes of *Opa-1***,** *Mitofilin*, *CHCHD3*, and *CHCHD6* knockout mice compared to WT. (**G**) Mitochondrial volume on log scale in myotubes of *Opa-1***,** *Mitofilin, CHCHD3*, and *CHCHD6* knockout mice compared to WT. Significance value **** $p \leq 0.0001$.

Supplementary:

Figure 1: The (**A**) volume (**B**) 3D area, and (**C**) perimeter of the average mitochondria in each of the three individual mice for the age cohorts, all shown on log scale. The (**D**) volume (**E**) 3D area, and (**F**) perimeter quantified on log scale with each dot representing one of the approximately 550 mitochondria analyzed for each age cohorts.

Figure 2: The (**A**) mitochondria branching index (MBI) and (**B**) sphericity of the average mitochondria in each of the three individual mice for the age cohorts. Combined data of mice for (**C**) MBI and (**D**) sphericity with each dot representing one of the approximately 550 mitochondria analyzed for each age cohorts.

Figure 3. Transcription of *Opa-1* and MICOS genes in aging mouse muscle. (**A-D**) Fold changes in the amount of OPA-1 and MICOS gene transcripts in mitochondria of myocytes of 3-month-old, 1-year-old, and 2-year-old mice as measured by RT-qPCR. (**A**) *Opa-1* transcripts. (**B**) *Mitofilin* transcripts. (**C**) *CHCHD3* transcripts. (**D**) *CHCHD6* transcripts. Significance values * $p \leq 0.05$, ** $p \leq 0.01$, *** $p \leq 0.001$, **** $p \leq 0.0001$.

Figure 4. (**A**) Metabolite PCA and (**B**) T-test comparing myotubes for control to *Mitofilin* knockout mice. (**C**) Heatmap showing the relative abundance of ions and (**D**) Enrichment analysis of metabolites, which links together several similarly functioning metabolites, with the relative abundance for *Mitofilin* knockout.

Figure 5. (**A**) Metabolite PCA and (**B**) ANOVA test comparing control to myotubes of *CHCHD3* and *CHCHD6* knockout mice (**C**) Heatmap showing the relative abundance of ions for control and (**D**) enrichment analysis metabolite for *CHCHD3* and *CHCHD6* knockout mice.

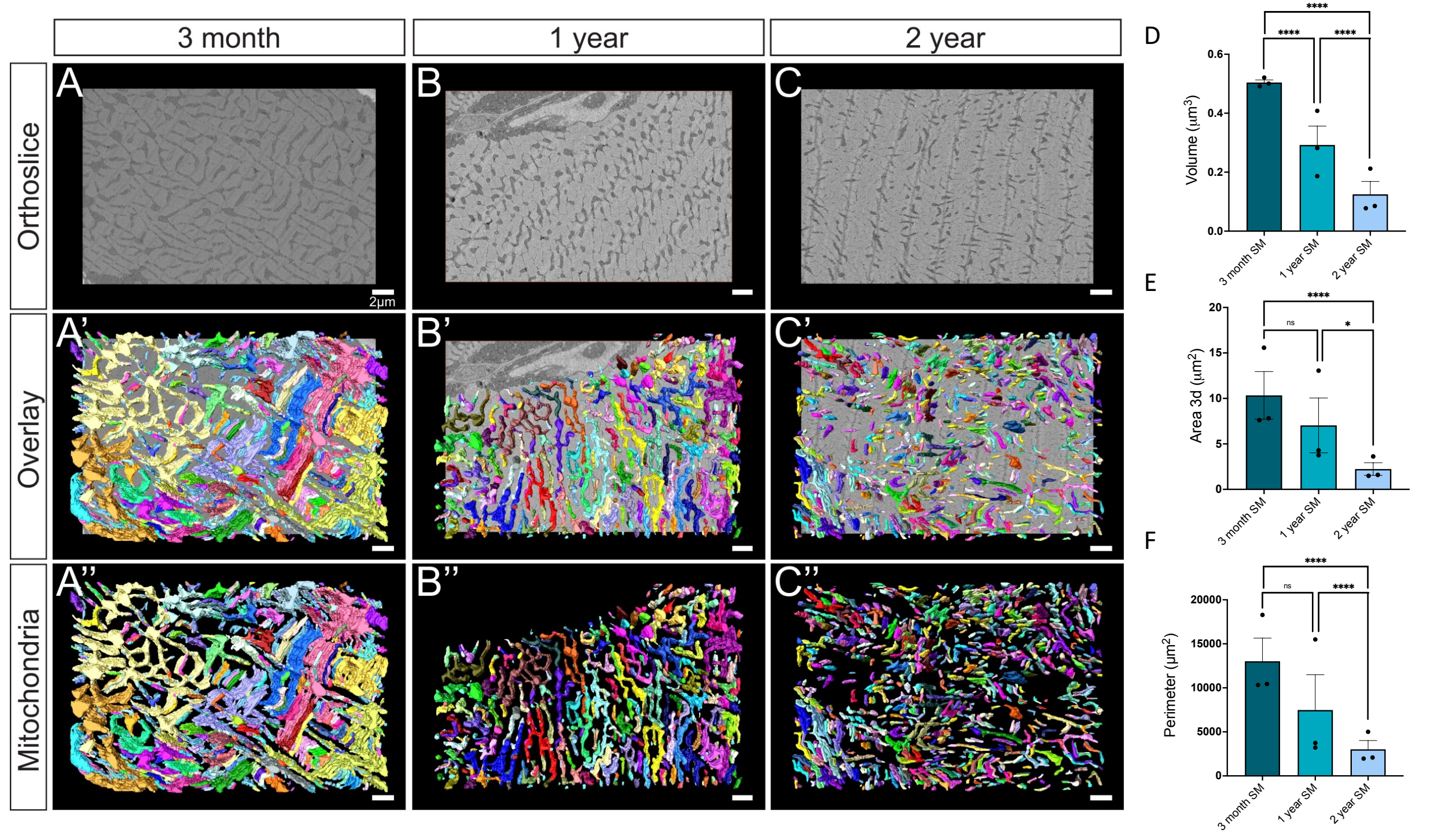
3 month
1 year
2 year
Orthoslice
Overlay
Mitochondria
A
B
C
2µm
A'
B'
C'
A''
B''
C''
D
Volume (µm3)
0.6
0.4
0.2
0.0
****
****
****
3 month SM
1 year SM
2 year SM
E
Area 3d (µm2)
20
15
10
5
0
****
ns
*
3 month SM
1 year SM
2 year SM
F
Perimeter (µm2)
20000
15000
10000
5000
0
****
ns
****
3 month SM
1 year SM
2 year SM

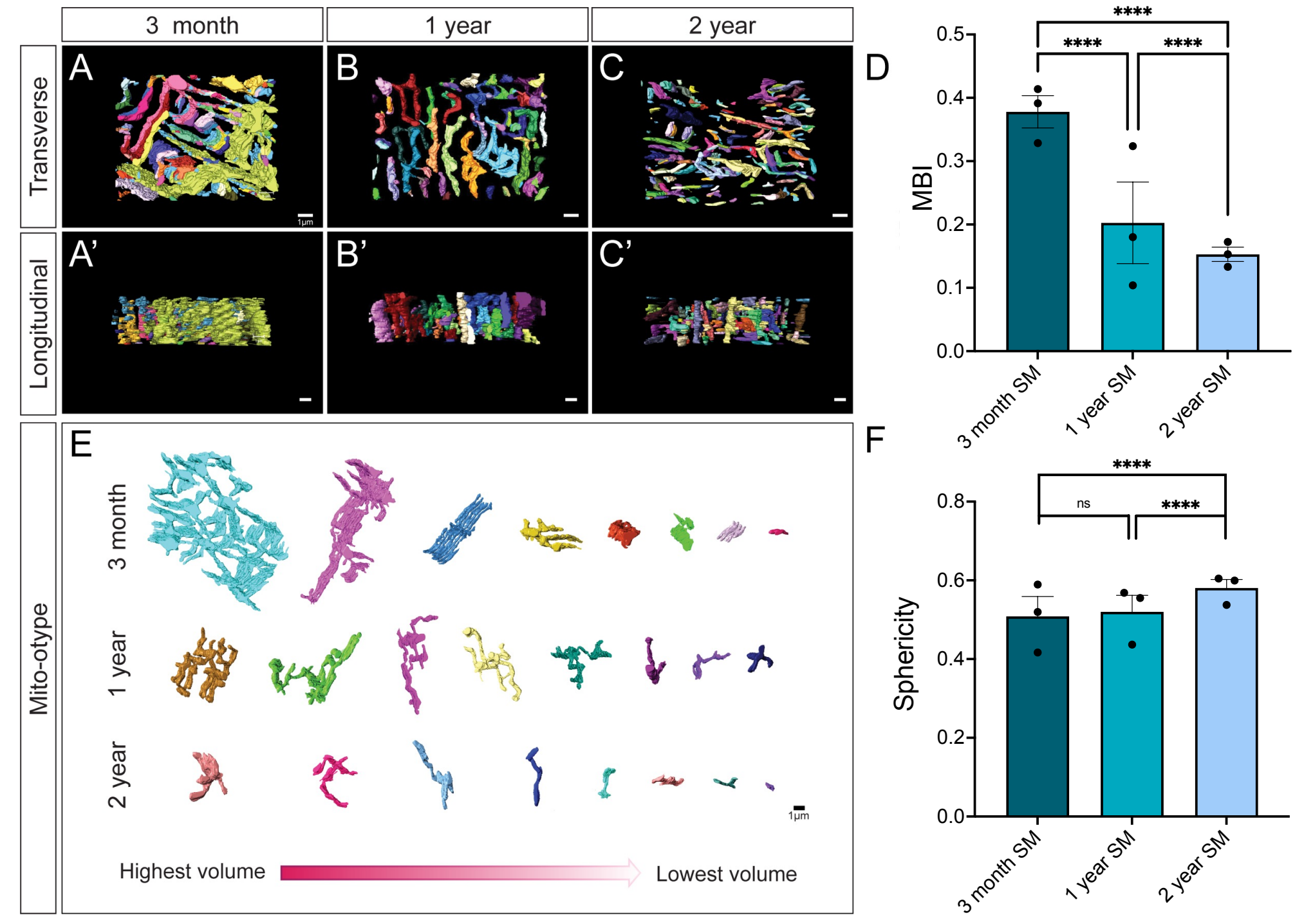
3 month
1 year
2 year
Transverse
Longitudinal
Mito-otype
A
B
C
A'
B'
C'
1µm
D
MBI
0.0
0.1
0.2
0.3
0.4
0.5
****
****
****
3 month SM
1 year SM
2 year SM
E
3 month
1 year
2 year
1µm
Highest volume
Lowest volume
F
Sphericity
0.0
0.2
0.4
0.6
0.8
****
ns
****
3 month SM
1 year SM
2 year SM

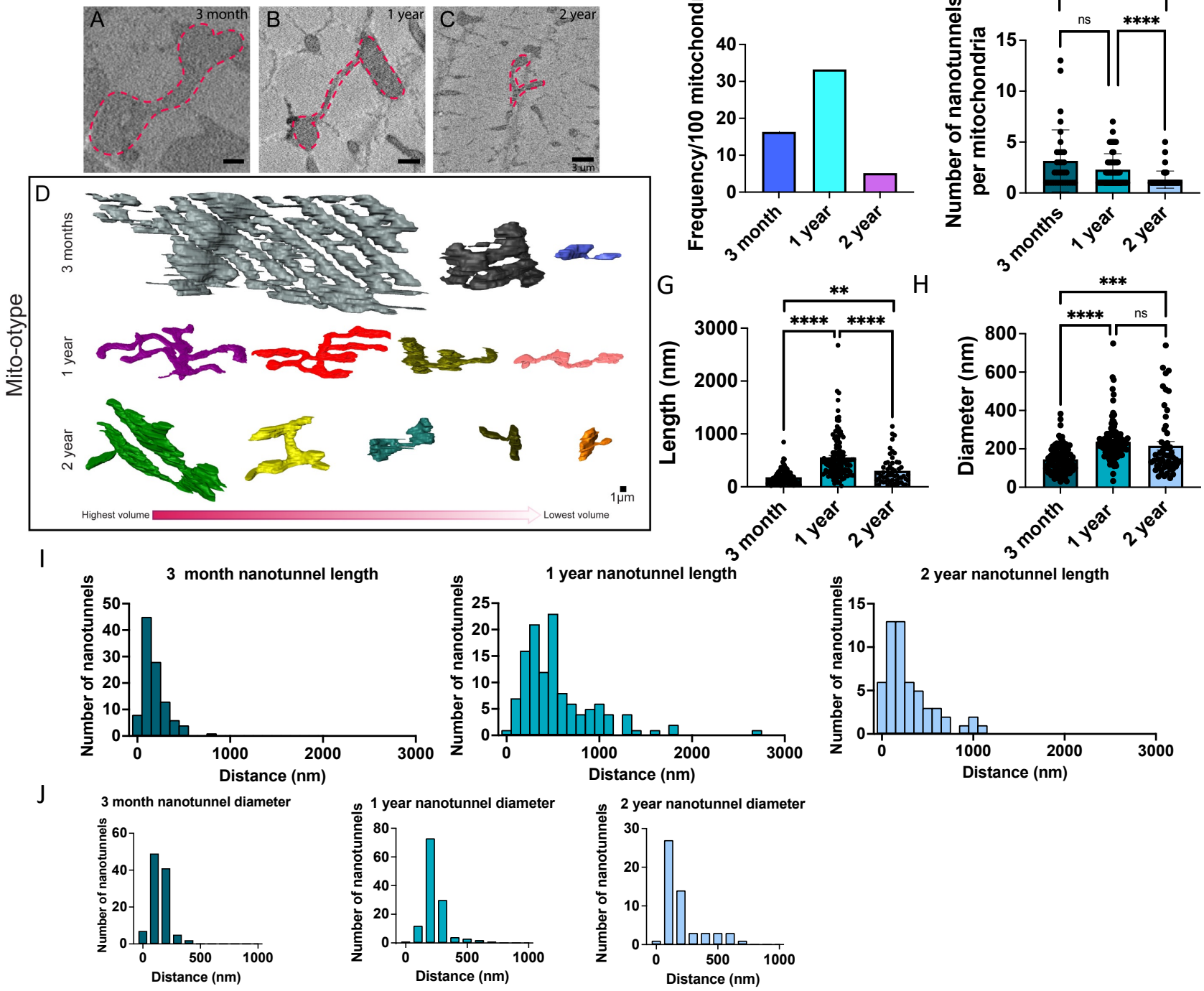
A
3 month
B
1 year
C
2 year
3 µm
D
Mito-otype
3 months
1 year
2 year
1µm
Highest volume
Lowest volume
E
Frequency/100 mitochondria
3 month
1 year
2 year
F
Number of nanotunnels per mitochondria
ns
****
****
3 months
1 year
2 year
G
Length (nm)
**
****
****
3 month
1 year
2 year
H
Diameter (nm)
***
****
ns
3 month
1 year
2 year
I
3 month nanotunnel length
1 year nanotunnel length
2 year nanotunnel length
Number of nanotunnels
Distance (nm)
J
3 month nanotunnel diameter
1 year nanotunnel diameter
2 year nanotunnel diameter
Number of nanotunnels
Distance (nm)

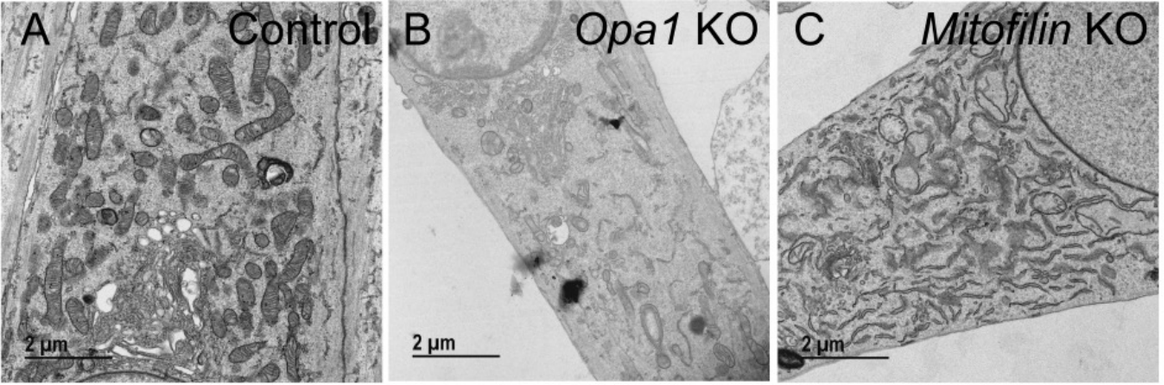
A
Control
2 µm
B
Opa1 KO
2 µm
C
Mitofilin KO
2 µm

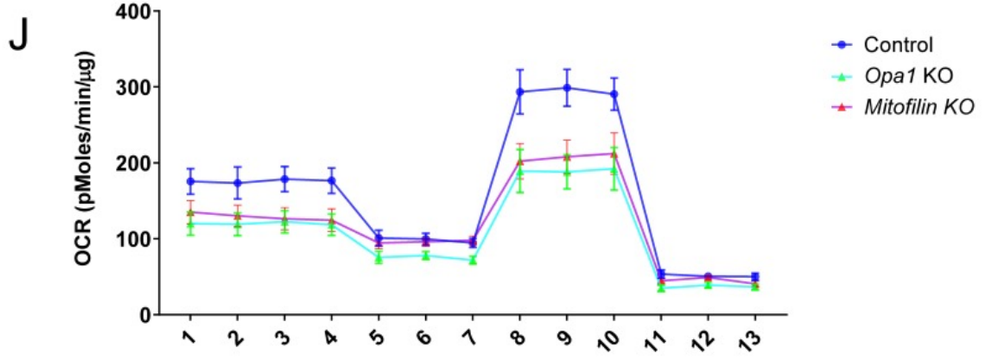
J
OCR (pMoles/min/µg)
400
300
200
100
0
1
2
3
4
5
6
7
8
9
10
11
12
13
Control
Opa1 KO
Mitofilin KO

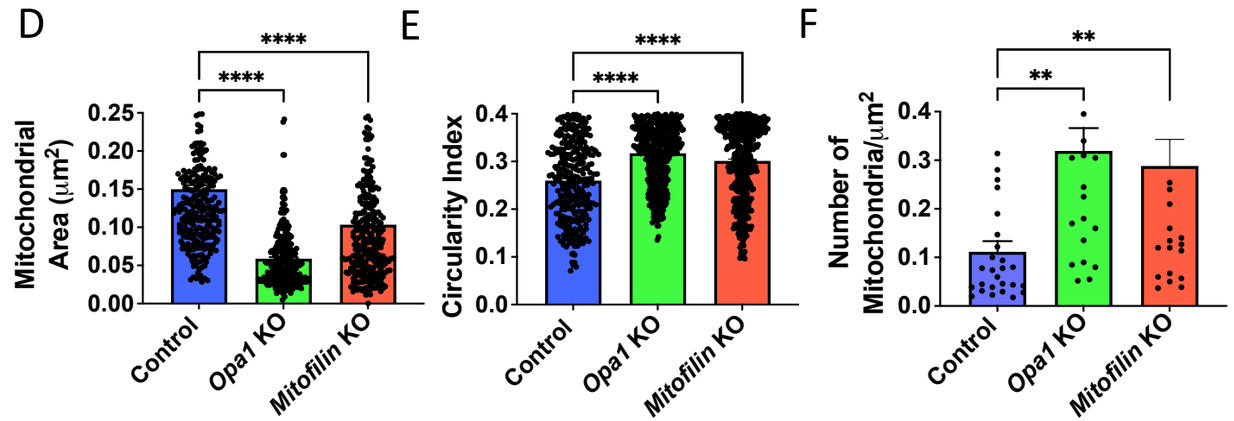
D
Mitochondrial Area (µm²)
0.25
0.20
0.15
0.10
0.05
0.00
****
****
Control
Opa1 KO
Mitofilin KO
E
Circularity Index
0.4
0.3
0.2
0.1
0.0
****
****
Control
Opa1 KO
Mitofilin KO
F
Number of Mitochondria/µm²
0.4
0.3
0.2
0.1
0.0
**
**
Control
Opa1 KO
Mitofilin KO

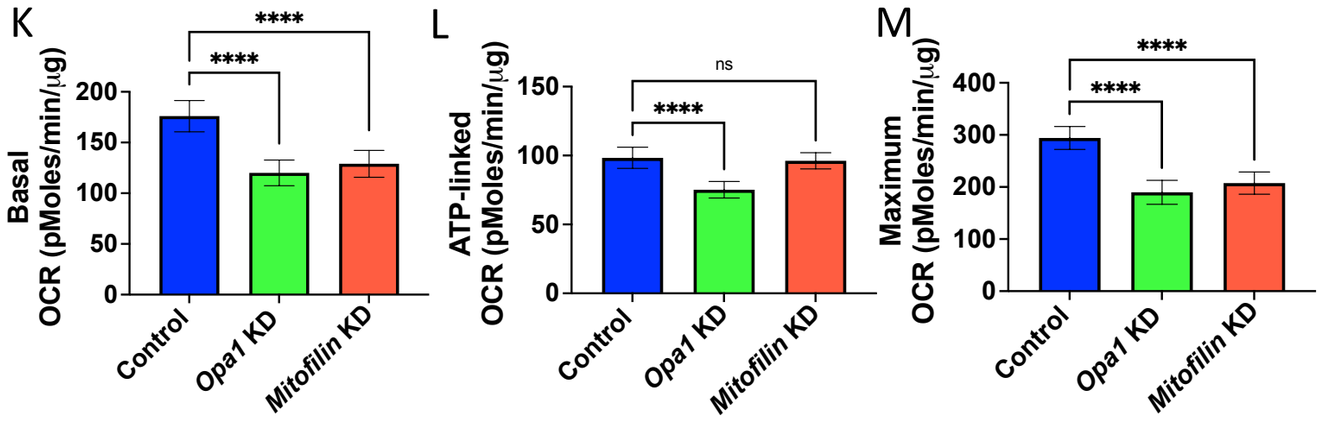
K
Basal OCR (pMoles/min/µg)
200
150
100
50
0
****
****
Control
Opa1 KD
Mitofilin KD
L
ATP-linked OCR (pMoles/min/µg)
150
100
50
0
ns
****
Control
Opa1 KD
Mitofilin KD
M
Maximum OCR (pMoles/min/µg)
400
300
200
100
0
****
****
Control
Opa1 KD
Mitofilin KD

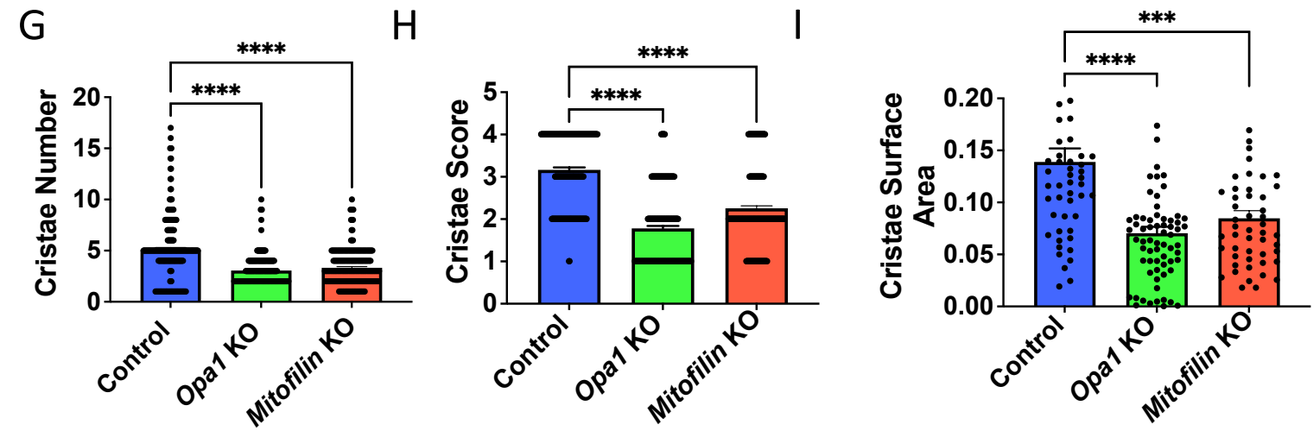
G
Cristae Number
20
15
10
5
0
****
****
Control
Opa1 KO
Mitofilin KO
H
Cristae Score
5
4
3
2
1
0
****
****
Control
Opa1 KO
Mitofilin KO
I
Cristae Surface Area
0.20
0.15
0.10
0.05
0.00
***
****
Control
Opa1 KO
Mitofilin KO

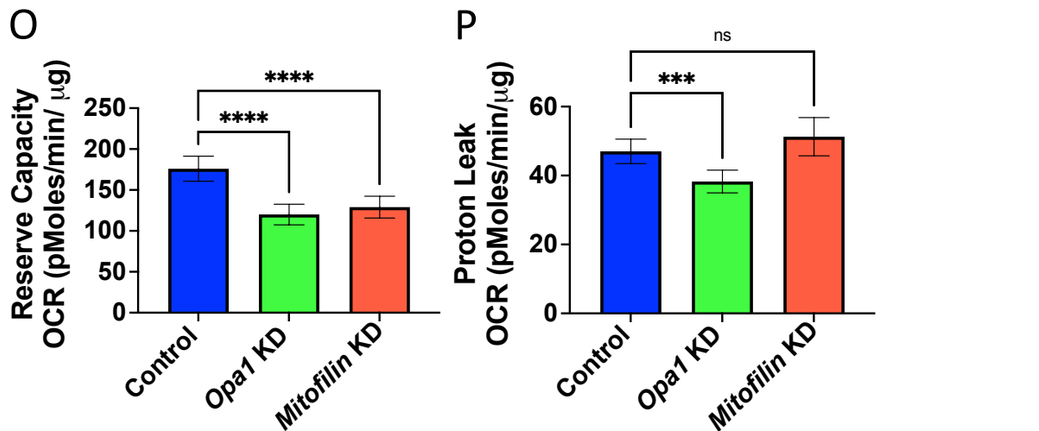
O
Reserve Capacity OCR (pMoles/min/ µg)
250
200
150
100
50
0
****
****
Control
Opa1 KD
Mitofilin KD
P
Proton Leak OCR (pMoles/min/µg)
60
40
20
0
ns
***
Control
Opa1 KD
Mitofilin KD

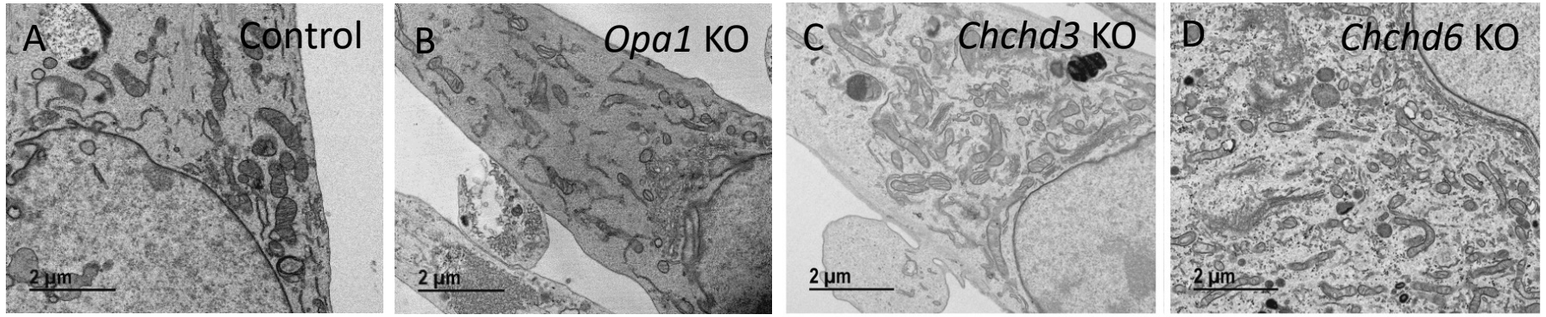
A
Control
B
Opa1 KO
C
Chchd3 KO
D
Chchd6 KO
2 µm
2 µm
2 µm
2 µm

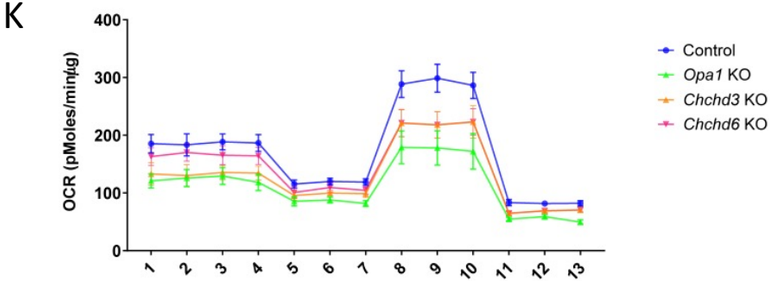
K
OCR (pMoles/min/µg)
Control
Opa1 KO
Chchd3 KO
Chchd6 KO

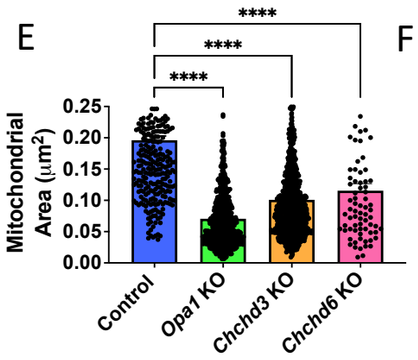
E
Mitochondrial Area (µm²)
Control
Opa1 KO
Chchd3 KO
Chchd6 KO

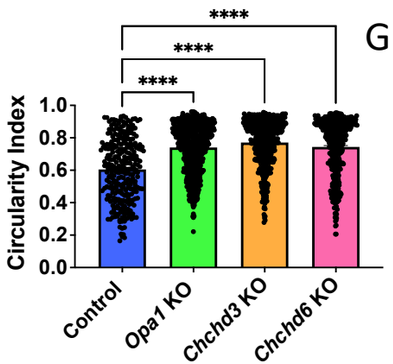
F
Circularity Index
Control
Opa1 KO
Chchd3 KO
Chchd6 KO

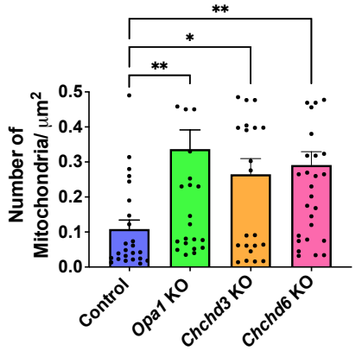
G
Number of Mitochondria/ µm²
Control
Opa1 KO
Chchd3 KO
Chchd6 KO

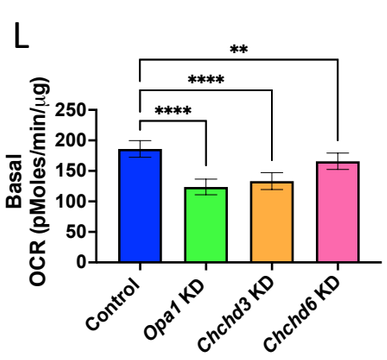
L
Basal OCR (pMoles/min/µg)
Control
Opa1 KD
Chchd3 KD
Chchd6 KD

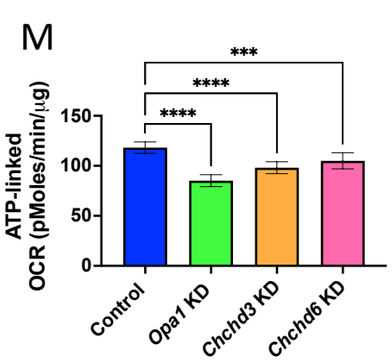
M
ATP-linked OCR (pMoles/min/µg)
Control
Opa1 KD
Chchd3 KD
Chchd6 KD

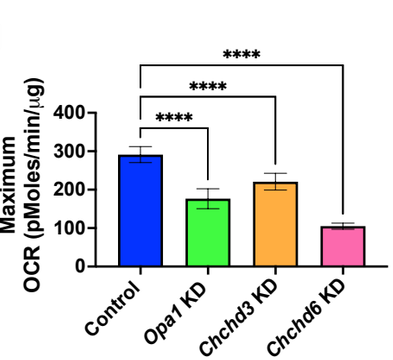
N
Maximum OCR (pMoles/min/µg)
Control
Opa1 KD
Chchd3 KD
Chchd6 KD

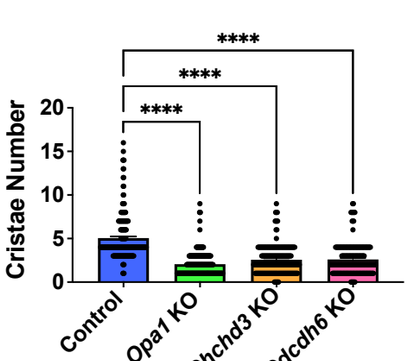
H
Cristae Number
Control
Opa1 KO
Chchd3 KO
Cdcdh6 KO

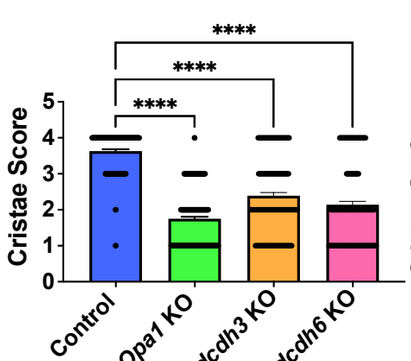
I
Cristae Score
Control
Opa1 KO
Cdcdh3 KO
Cdcdh6 KO

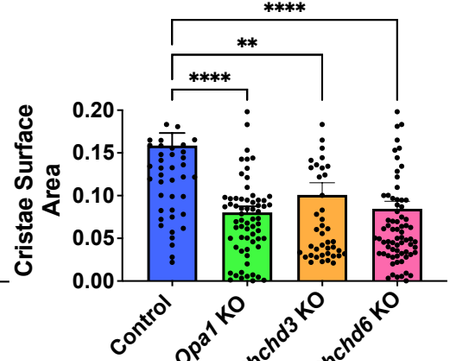
J
Cristae Surface Area
Control
Opa1 KO
Chchd3 KO
Chchd6 KO

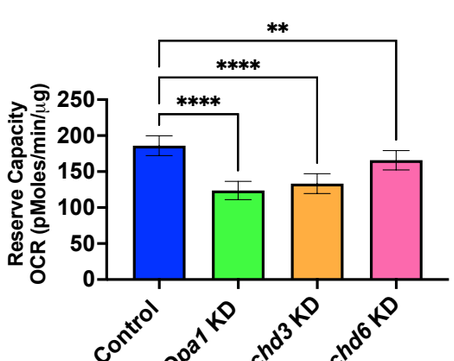
O
Reserve Capacity OCR (pMoles/min/µg)
Control
Opa1 KD
Chchd3 KD
Chchd6 KD

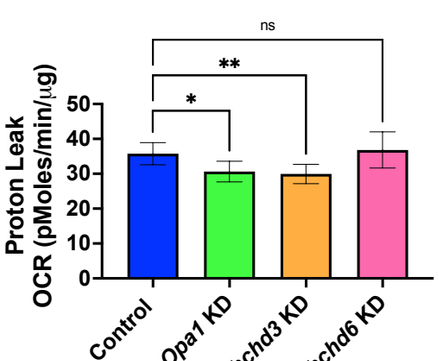
P
Proton Leak OCR (pMoles/min/µg)
ns
Control
Opa1 KD
Chchd3 KD
Chchd6 KD

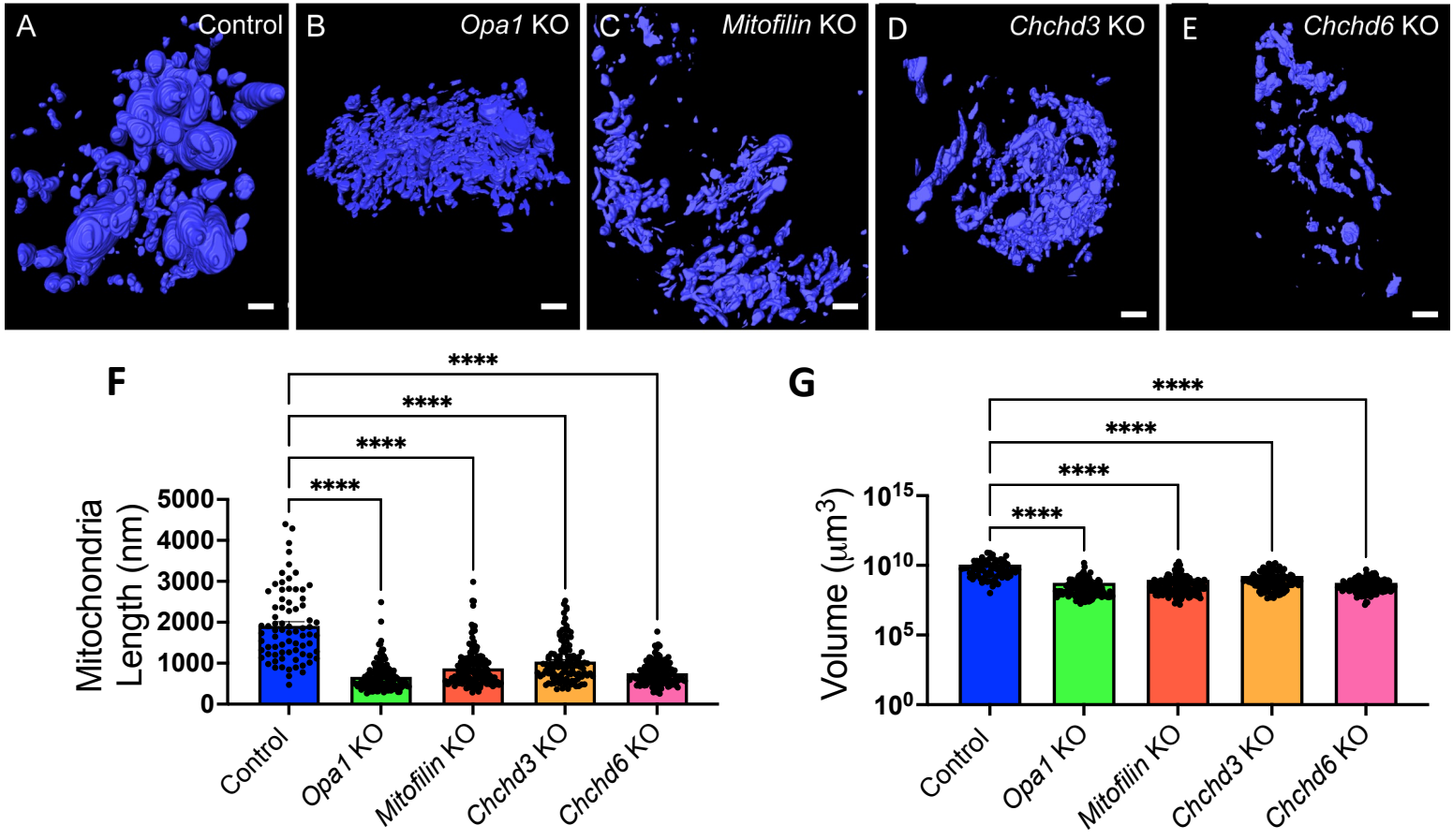
A
Control
B
Opa1 KO
C
Mitofilin KO
D
Chchd3 KO
E
Chchd6 KO
F
Mitochondria Length (nm)
5000
4000
3000
2000
1000
0
****
****
****
****
Control
Opa1 KO
Mitofilin KO
Chchd3 KO
Chchd6 KO
G
Volume (μm3)
10^15
10^10
10^5
10^0
****
****
****
****
Control
Opa1 KO
Mitofilin KO
Chchd3 KO
Chchd6 KO